MilliporeSigma

Material Matters™

VOLUME 16 • NUMBER 2

Advances in Nanomaterials: Bioassays and Imaging

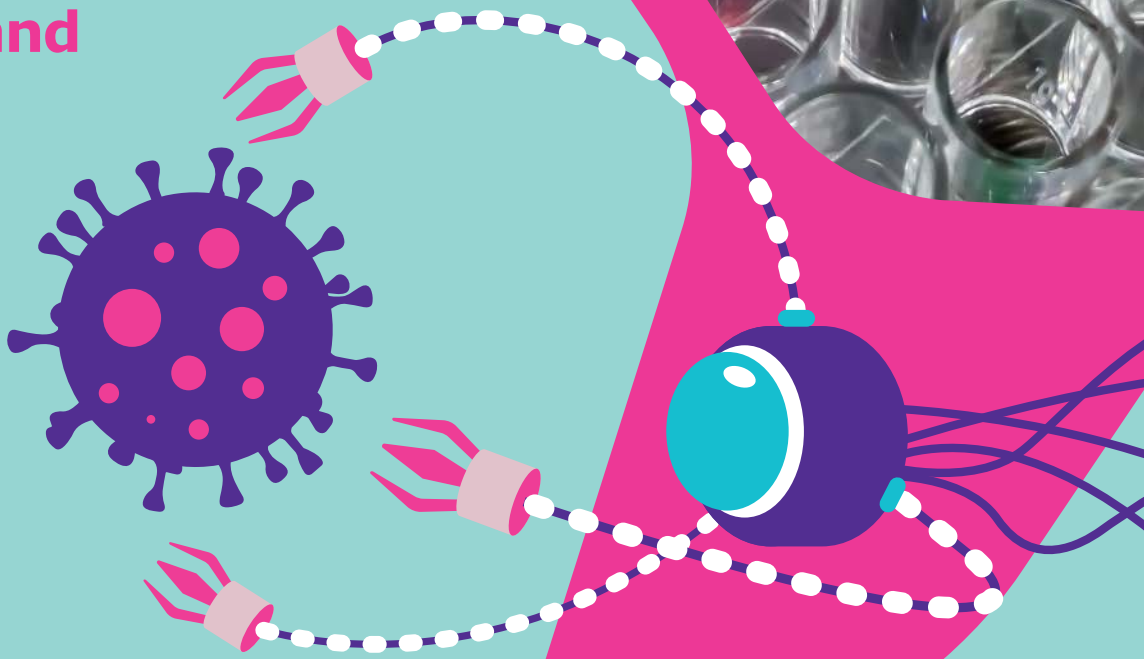

Material Matters™
VOL. 16 • NO. 2

Introduction

Megan Muroski, Ph.D
Global Product Manager - Nanomaterials and Energy

Welcome to issue 16.2 of *Material Matters*™, Advances in Nanomaterials: Bioassays and Imaging. This issue highlights recent trends associated with new material discoveries related to bioimaging, assays, diagnostics, and magnetic imaging.

In our first article, **Dr. Delehanty** and researchers from the Naval Research Laboratory and the University of Maryland introduce recent advances in the use of cadmium-free quantum dots for bioimaging. They focus on strategies that have emerged in the last five years in the design, synthesis, and surface modifications for non-Cd quantum dots (QDs) for bioimaging and sensing applications. The challenges of improving colloidal stability, biocompatibility, and targeting in Cd-free QD configurations, such as indium phosphide (InP) and copper indium sulfide ($CuInS_2$ QD), are discussed.

Dr. David Medina Cruz et. al. investigate advances in noble bimetallic nanoparticles (BMNP) to more precisely measure and monitor glucose levels in the blood. This review focuses on the use of enzyme-free silver (Ag) and gold (Au) nanoparticles, such as Ag-Au, Ag-Pt, Ag-Pd, and Au-Pt, and how their structures contribute to biosensor detection. These nanomaterials allow for flexibility in detection, range, and sensitivity, which are essential for clinical translation to better manage diabetes.

In our third article by **Professor Fujita** and colleagues from Osaka University and the RIKEN Cluster for Pioneering Research, recent progress in metallic nanoparticles for bioimaging and molecular spectroscopy of biological systems is discussed. Metallic nanoparticles lend themselves to many applications in this field, including spatio-temporal tracking with microsecond time resolution, as well as multicolor imaging using the surface plasmon resonance properties of silver and gold nanoparticles. In addition to detection, the authors discuss the use of metallic nanoparticles in SERS probes for drug uptake, pH sensing, and live-cell tracking.

Exploring the use of nanomaterials in bioassays would not be complete without investigating the effects of gold nanoparticles. **Drs. Fernandes and Baptista** explore the synthesis and functionalization of gold nanoparticles and their use in molecular diagnostics, focusing on lateral flow assays. Due to the growing use of gold nanoparticles in these systems, they further discuss the regulations and standards of these materials, as well as the future outlook and challenges that remain in integrating gold nanoparticles into the mainstream.

In our final article, **Professor Yu Cheng** and co-workers at the Tongji University School of Medicine look at the recent advances of nanoparticle-based imaging contrast agents for *in vivo* stem cell tracking. This review provides an in-depth look at popular *in vivo* imaging techniques, magnetic resonance imaging, fluorescence imaging, ultrasound imaging, and photoacoustic imaging. The authors describe the advantages and disadvantages of these techniques and state-of-the-art nanoagents in the biomedical field.

Each article in this publication concludes with a list of relevant SigmaAldrich materials available from MilliporeSigma. For additional product information, please visit us at **SigmaAldrich.com/matsci**. If you have any new product suggestions, questions or comments, or new ideas for future *Material Matters*™ issues, please contact us at **SigmaAldrich.com/technicalservice**.

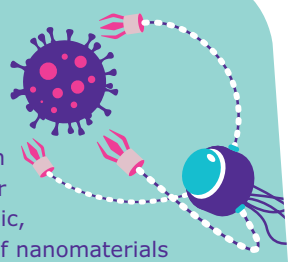

About the Cover

Nanotechnology is based upon the fundamental research that generates new types of nanoparticles that are fit for a huge variety of applications. The highly-tuned electronic, magnetic, optical, catalytic, and mechanical properties of nanomaterials have resulted from an interdisciplinary effort to study their ability to interact with biomaterials. As depicted in this cover art, the comparably sized nanoparticles and biomaterials interact to improve the sensitivity and flexibility of current detection techniques. Our Materials Science team is dedicated to advance the knowledge of nanomaterial technologies with a comprehensive portfolio of innovative materials to empower breakthroughs.

Merck KGaA, Darmstadt, Germany
Frankfurter Strasse 250
64293 Darmstadt, Germany
Phone +49 6151 72 0

To Place Orders / Customer Service
Contact your local office or visit
SigmaAldrich.com/order

Technical Service
Contact your local office or visit
SigmaAldrich.com/techinfo

General Correspondence
Contact your local office or visit
SigmaAldrich.com/techinfo

Subscriptions
Request your FREE subscription to *Material Matters*™ at **SigmaAldrich.com/mm**

The entire *Material Matters*™ archive is available at **SigmaAldrich.com/mm**

Material Matters™ (ISSN 1933-9631) is a publication of Merck KGaA, Darmstadt, Germany

Table of Contents

Articles

Featured Products

Your Material Matters

Bryce P. Nelson, Ph.D.
Materials Science Initiative Lead

We welcome novel product ideas! Do you have a material or compound that should be featured in our Materials Science portfolio? If it is needed to accelerate your research, it matters. Send your suggestion to SigmaAldrich.com/techinfo for consideration.

Selenium nanoparticles (SeNP) have recently emerged as an exciting new tool for use with many biological systems, as selenium demonstrates antimicrobial, anticancer, and antioxidant properties.[1] The development of selenium nanoparticles has gained considerable focus in biomedical and food science applications due to their low toxicity and high biocompatibility. As a trace mineral essential for human health, SeNP also exhibits excellent optical, photoelectric, and photoconductive properties and is used in advanced material formulations.[2]

The multidimensional applications of selenium nanoparticles, by Dr. Hanrahan and co-workers from Glantreo Limited, appeared as a new technical spotlight on SigmaAldrich.com in 2021 and discusses the use of these novel particles.[3] SeNP are used in many biomedical applications, including COVID-19 diagnostic sensors, medical devices, anticancer antidiabetic, anti-inflammatory, and antimicrobial uses. In addition, SeNP can be found in applications for food supplements, solar cells, cosmetics, and agricultural/ fertilization. Collaborative efforts are still needed to broaden the current knowledge about biogenic SeNPs and better address their function in these therapeutic and environmental areas.

References:

(1) Vahdati, M.; Tohidi Moghadam, T. *Sci. Rep.* **2020**, *10*, 510. https://doi.org/10.1038/s41598-019-57333-7
(2) Vinković Vrček I. (**2018**) *Selenium Nanoparticles: Biomedical Applications.* In: Michalke B. (eds) Selenium. Molecular and Integrative Toxicology. Springer, Cham. https://doi.org/10.1007/978-3-319-95390-8_21
(3) SigmaAldrich.com Glantro Technical Article *Multidimensional Application of Selenium Nanoparticles*

Name	Particle size (mm)	Cat. No.
Selenium nanoparticles, 0.15 wt. % in water, dispersion	80	**919519-1ML**
	150	**919527-1ML**
	250	**919659-1ML**

MilliporeSigma

THE FUTURE OF BIOIMAGING

Nanomaterial Bioconjugation Techniques

A guide for surface modification allowing bioconjugation of inorganic nanomaterials having applications in theranostics. Discover the latest advances and protocols in nanoparticle conjugation for:

- Magnetic Imaging
- Fluorescence Imaging
- Optical-based Imaging

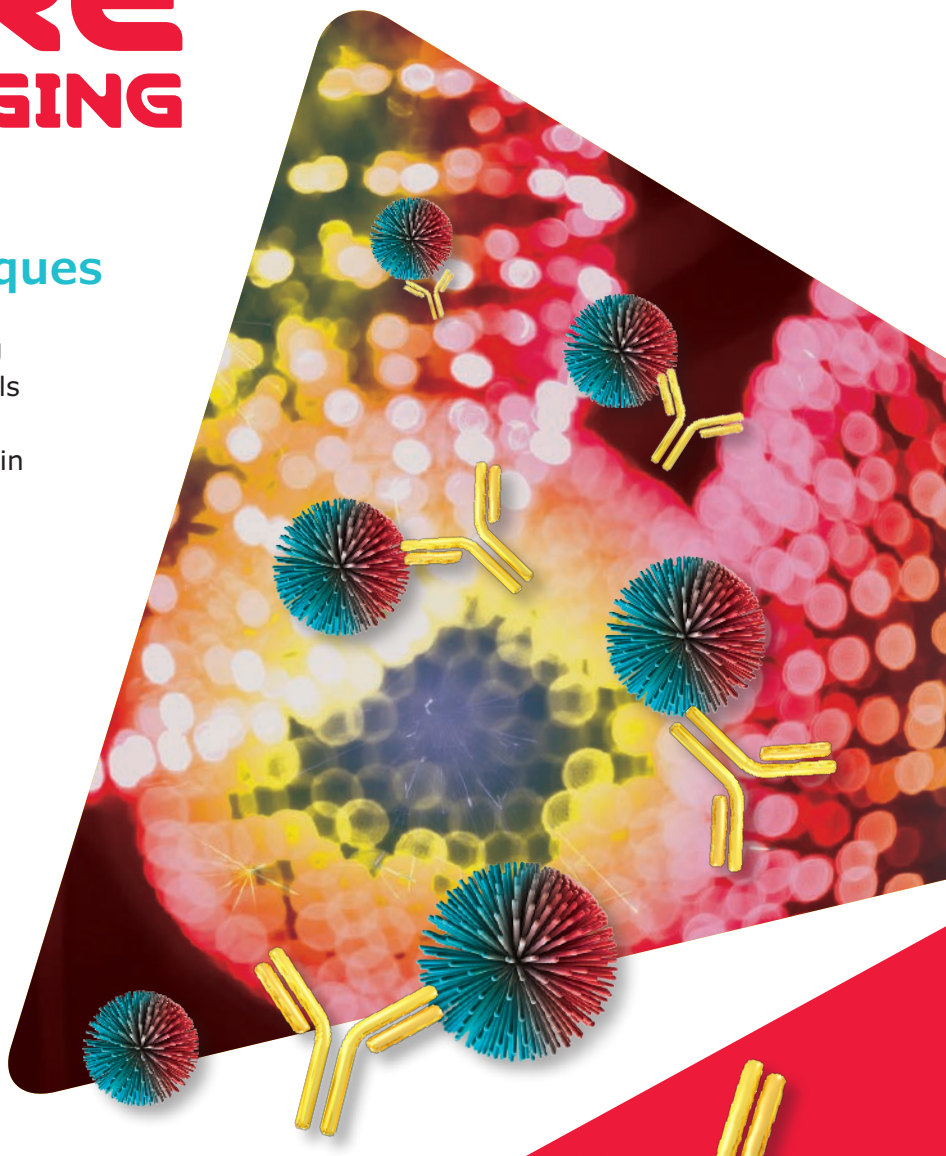

Order your complimentary copy from:
SigmaAldrich.com/nanomaterials-conjugation

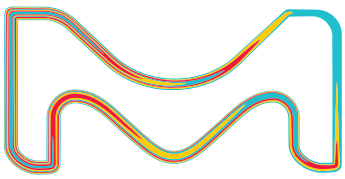

Sigma-Aldrich®
Lab & Production Materials

Recent Advances in the Use of Cadmium-free Quantum Dots for Bioimaging




Katherine E. Rogers,[1,2] Okhil K. Nag,[1] Michael H. Stewart,[1] James B. Delehanty[1*]

[1] Center for Bio/Molecular Science and Engineering, Code 6900, U.S. Naval Research Laboratory, Washington, DC 20375
[2] Fischell Department of Bioengineering, 2330 Kim Engineering Building, University of Maryland, College Park, MD 20742
* Email: james.delehanty@nrl.navy.mil

Introduction

Quantum dots (QDs) are nanometer-sized (2–10 nm) semiconducting crystalline materials that exhibit size-dependent optoelectronic properties. Most notably, the wavelength of their photoluminescence (PL) emission tracks directly with the size of the material as synthesized. In the last few decades, QDs have garnered tremendous attention as nanoparticle (NP) platforms for various applications in electronic devices, bioimaging, biosensing, and drug delivery due to their unique features. Among the many outstanding optical properties of QDs, their large absorption coefficients, narrow emission bands, large stoke shifts, high PL quantum yield (QY), and excellent photostability are highly advantageous for biological imaging.[1] For example, a sample can be labeled with different sized QDs and excited with a single excitation source far removed to the ultraviolet portion of the spectrum to produce distinct bright emission colors in the visible, making QDs particularly suitable for multiplexed imaging. QDs can be coated with different hydrophilic surface ligands with functional chemical groups (e.g., carboxylic acid, amine) to impart colloidal stability in aqueous environments and to facilitate conjugation to biologicals (peptides, polymers, and ligands), dyes, and drugs.

QDs for biological applications typically consist of a core/shell structure capped with hydrophilic ligands. To date, QD systems based on CdSe/ZnS structures have been the primary focus of researchers due to ease of synthesis and post-synthesis surface modification. Typically, the core of these QDs are composed of elements from groups II-VI (e.g., CdTe and CdSe), with a shell composed of ZnS. The shell protects against degradation of the core and maintains QD PL while also serving as an anchor point for ligand attachment. However, despite numerous studies demonstrating the stability and the largely innocuous nature of Cd-based QD systems *in vitro* and *in vivo*,[2–4] concerns regarding the long-term persistence of Cd-containing QDs and associated heavy metal-induced toxicity have spurred interest in the development of alternative QD configurations. Over the last decade, many research groups have focused on developing fabrication methods to synthesize different sized Cd-free QDs with various core/shell configurations and surface coatings. Here, the primary focus has been developing biocompatible Cd-free QDs with optoelectronic and surface properties comparable to existing Cd-based QDs. Among the various non-Cd QDs developed, indium phosphide (InP), copper indium sulfide ($CuInS_2$), and graphene QDs have been highly studied for biosensing and bioimaging applications. Although many properties of these non-Cd QDs are comparable to the Cd-based QDs, their surface chemistry and colloidal and optical stability in physiological environments have lagged behind that of Cd QDs. This review provides a snapshot of the current state of the art for the design, synthesis, and surface modification strategies for non-Cd QDs for use in bioimaging and sensing applications. We focus our discussion on the progress made in the last 5 years and highlight the critical challenges to overcome to advance this field further.

Structural Constructions of Cd-free QDs

Like Cd-based QDs, Cd-free QDs also have a size range of 2–10 nm and are comprised of core/shell architectures. However, Cd-free QD cores are typically comprised of elements from groups III–V (e.g., InP) (**Figure 1**). These cores, particularly InP, are structurally more robust and stable due to covalent bonds in their matrix.[5,6] However, the PL intensity and QY of these cores have generally been lower than Cd-containing core QDs. Several studies have used shell coatings with a broader bandgap material to overcome this challenge, such as ZnS and/or ZnSe layers. These shell coatings 1) reduce interactions between the exciton and the outer surface of the core nanocrystal to minimize surface defects and quenching, 2) facilitate better control of emission wavelength, PL lifetime, and QY, and 3) enhance chemical reactivity for ligand exchange. Based on the core/shell combination and band alignment of the valence and conduction bands of the constituent materials, these QDs can be divided into three types (i.e., type I, type II, and quasi type II), described elsewhere.[7] In general, type I core/shell QDs possess a conduction band of the shell at higher energy than that of core, whereas the valence band of the shell is at lower energy relative to the core. Cd-free type I core/shell QDs, such as InP/ZnS, $CuInS_2$/ZnS, $AgInS_2$/ZnS, and ZnSe/ZnS, have been widely developed for various biological applications (**Figure 1**).[8] In the following section, we discuss some of these examples and highlight their contribution to developing Cd-free QDs for bioimaging and sensing.

Bioimaging and Sensing with InP and $CuInS_2$ QDs

InP/ZnS has emerged as the most popular type of Cd-free QD for use in bioimaging.[9] Wu et al. conjugated InP/ZnS QDs to an anti-vascular endothelial growth factor receptor-2 (VEGFR-2) monoclonal antibody and loaded them with miR-92A miRNA to inhibit proliferation of cancerous myeloid cells.[10] In this way, they produced a bifunctional InP nanocomposite (IMAN) for targeted imaging and therapy. In K562 leukemia cell models examined using near-infrared (NIR) imaging, the IMAN fluoresced and localized to the plasma membrane before entering the cells (**Figure 2Ai**). The researchers also demonstrated that greater doses of IMAN incubated with K562 cells for 36 hours led to more efficient cell killing than InP QDs or miR inhibitor alone (**Figure 2Aii**). *In vivo*, the use of the VEGFR-2 had a significant effect on the specificity of tumor localization. K562 tumor-bearing nude mouse models were given tail vein injections of phosphate-buffered saline (PBS), 10 mg/kg InP QDs, or 10 mg/kg IMAN and tracked using NIR imaging (**Figure 2Aiii**). Notably, while InP QDs were diffusely located within the abdomen, only IMAN localized to the tumor site. Further, the group showed that a consistent intravenous treatment of 10 mg/kg IMAN over 20 days led to significantly higher tumor volume reduction within the mouse model than the free miR-92a inhibitor (**Figure 2Aiv**).

Similarly, $CuInS_2$-based QDs have also emerged as another platform for developing heavy metal-free QDs for bioimaging. Yang et al. used 2-[bis[2-[carboxymethyl-[2-oxo-2-(2 sulfanylethylamino) ethyl]amino]ethyl]amino]acetic acid (DTDTPA)-modified $CuInS_2$/ZnS QDs chelated with gadolinium ions (for MRI) for a bimodal imaging nanoparticle (QDs@DTDTPA-Gd NPs) capable of use with NIR fluorescence or magnetic resonance imaging (MRI) (**Figure 2Bi**).[11] DTDTPA was chosen due to its water solubility and ability to chelate gadolinium while being able to attach to the shell of the QD. Within a HeLa-tumor bearing nude mouse model, increasing magnetic resonance signal intensity was observed within the tumor over 48 hours, subsequent to an intravenous dose of 20 mg/kg QDs@DTDTPA-Gd NPs (**Figure 2Bii**). A similar increase in fluorescence intensity from the QD was also observed (**Figure 2Biii**). Encouragingly, organs harvested from sacrificed mice after 48 hours showed that QDs@DTDTPA-Gd NPs localized primarily to the liver, tumor, and spleen via passive targeting accumulation (**Figures 2Biv, 2Bv**).

Another research team applied $CuInS_2$/ZnS QDs embedded within a glycol-chitosan matrix (GCM). After coating with 11-mercaptoundecanoic acid (MUA) to prime for use in aqueous solutions, conjugation of the composite to RGD peptides for improved tumor targeting to produce cRGDyk-GCM-QDs

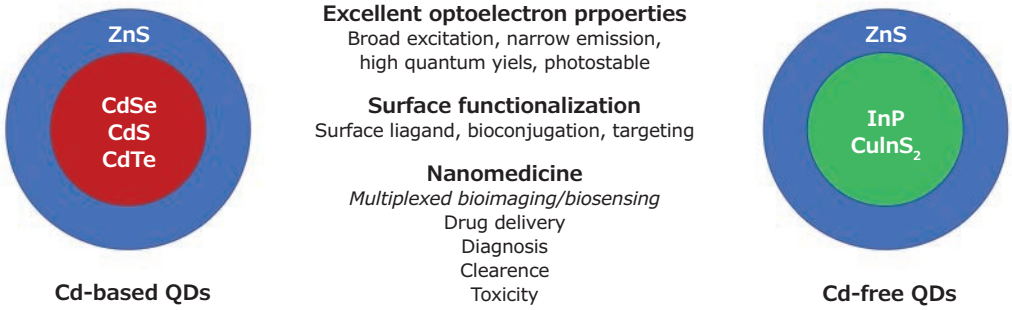

Figure 1. Cd-based vs. Cd-free QDs for applications in nanomedicine. Core/shell QDs based on Cd cores (CdSe, CdS, CdTe) with ZnS have been the prototypical platform for QD-based sensing and imaging. More recently, QDs based on non-Cd cores such as InP and $CuInS_2$ are being investigated as Cd-free options for these applications.

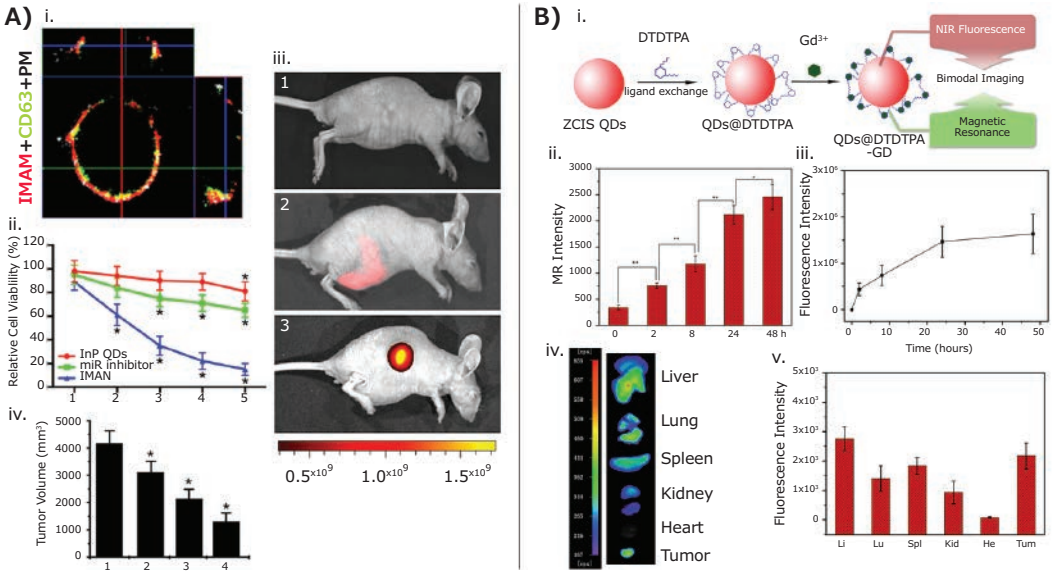

Figure 2. Examples of InP and $CuInS_2$-based QDs used for bioimaging. **A**) (**i**) K562 cells treated *in vitro* with 10 mg/L IMAN (red), Alexa 488-conjugated anti-CD63 antibody (green), and Dil (white) showing localization of IMAN to the plasma membrane. (**ii**) Relative cell viability of K562 cells *in vitro* after 36 hours of treatment, analyzed via MTT assay. The lower axis shows concentration. For IMAN and InP QD treatment, concentrations (1–5) were 0.01, 0.1, 1, 10 and 50 mg/L respectively. For miR-92a inhibitor treatment, concentrations (1–5) were 0.001, 0.01, 0.1, 1 and 5 mg/L respectively. (∗, $P < 0.05$). (**iii**) NIR imaging of K562 tumor-bearing mouse 1 hour after intravenous tail injection. **1**) mouse injected with PBS; **2**) mouse treated with 10 mg/kg InP QDs; **3**) mouse treated with 10 mg/kg IMAN. The color bar displays NIR fluorescence intensity units. (**iv**) K562 xenograft tumor volume in nude mice after intravenous treatment every 2 days with (1) PBS (control), (2) 10 mg/kg InP QDs, (3) 1 mg/kg miR-92a inhibitor, or (4) 10 mg/kg IMAN for 20 days. (∗, $P < 0.05$). Image adapted with permission from reference 10, copyright 2017 American Chemical Society2017. **B**) (**i**) Schematic of fabrication of QDs@DTDTPA-Gd NPs from $CuInS_2$/ZnS QDs (ZCIS QDs). (**ii**) Magnetic resonance signal intensities of nude mice with HeLa xenograft tumors 0, 8, 24, and 48 hours after tail vein injection of 20 mg/kg QD@DTDTPA-Gd NPs. (∗, $p < 0.05$; **, $p < 0.01$) (**iii**) Quantified fluorescence intensity (photon counts in tumor per 150 mm^2) of the tumors in HeLa-xenograft nude mice at 0, 2, 8, 24, and 48 hours after tail vein injection of 20 mg/kg QDs@DTDTPA-Gd NPs. (**iv**) Fluorescence images of *ex vivo* organs from HeLa-xenograft tumor-bearing nude mice, 48 hours after a tail vein injection of 20 mg/kg QDs@DTDTPA-Gd NPs. (**v**) Fluorescence quantification of *ex vivo* organs from HeLa-xenograft tumor-bearing nude mice, 48 hours after a tail vein injection of 20 mg/kg QDs@DTDTPA-Gd NPs. (Legend: Li, Liver; Lu, Lung; Spl, Spleen; Kid, Kidney; He, Heart; Tum, Tumor). Image adapted from reference 11, copyright 2017 American Chemical Society.

(**Figure 3Ai**).[12] Examination of *in vitro* cell viability for GCM-QDs and MUA-QDs using an MTT assay found no significant loss in viability. *In vivo*, the researchers used MRI fluorescence imaging to observe localization of intravenously injected cRGDyk-GCM-QDs at the site of the subcutaneous RR1022 xenograft tumor within nude mice (**Figure 3Aii**).

Bioimaging and Sensing with Other Types of Cd-free QDs

Literature reports other Cd-free QD configurations, such as an InP core. For example, Zhang et al., formulated an oil-soluble InP/ZnSe/ZnS core/multi-shell QD. This InP/ZnSe/ZnS QD is unique in its ability to emit at two distinct wavelengths with peak emissions in the visible and near-infrared (NIR) (**Figures 3Bi, ii**).[13] The surface of the InP/ZnSe/ZnS QDs was modified with a poly(acrylic acid)-octylamine amphiphilic (PAA) polymer grafted with an Arg-Gly-Asp (RGD) peptide for water solubility and tumor localization. Within a Bcl-7402 tumor-bearing mouse model, the PAA polymer/RGD-modified QDs were visually located at the tumor site using NIR fluorescence within one hour after intravenous injection of a 1 mg/mL solution of QDs (**Figure 3Biii**). The control MCF-7 tumor-bearing mouse model, which lacks the protein targeted by RGD, did not exhibit targeted localization to the tumor site. The case of the Bcl-7402 mouse model treated with QDs lacking the RGD modification obtained similar results.

Although used less commonly than InP/ZnS and $CuInS_2$/ZnS QDs, the adaptation of other types of Cd-free QDs found use in physiological applications. Zn-doped $AgInS_2$ (AIZS) QDs were utilized by Zang et al. to create biocompatible AIZS-graphene oxide (AIZS-GO) nanocomposites.[14] To produce these, oleylamine-modified GO was assembled to AIZS QDs using thermal decomposition and mini emulsion (**Figure 3Ci**). Incubation of the AIZS-GO nanocomposites occurred in SK-BR-3 breast cancer cells, and proliferation assay (MTT) accessed the cell viability. At 0.8 μg/mL, the cells retained 84% viability, suggesting acceptable biocompatibility and low cytotoxicity of the AIZS-GO nanocomposites (**Figure 3Cii**). The group further demonstrated a brief *in vivo* proof of ability to optically image and distinguish the AIZS-GO nanoparticles within a SK-BR-3 cancer cell-bearing mouse model (**Figure 3Ciii**). QDs based on ZnSe core structures are another Cd-free alternative. Zhou et al. used manganese-doped ZnSe QDs as a dual MRI/fluorescent imaging probe.[15] These Mn-ZnSe QDs were loaded into mesoporous silica particles to create MSN@QDs (**Figure 3Di**) that were further decorated with a tumor-targeting

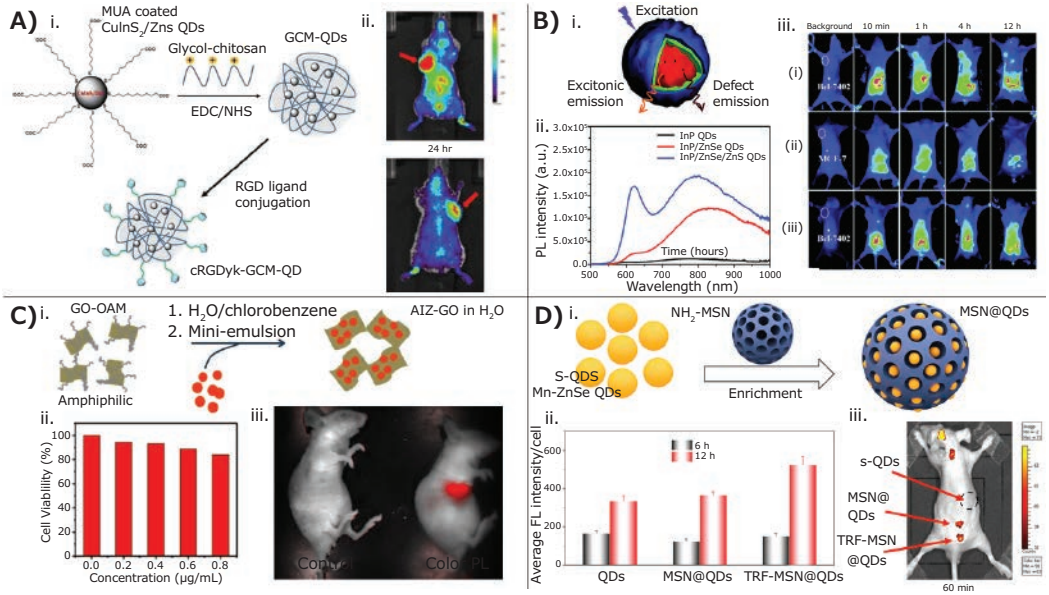

Figure 3. Bioimaging applications for various types of Cd-free QDs. **A**) (**i**) Schematic of the composition of cRGDyk-GCM-QDs. MUA-coated $CuInS_2$/ZnS QDs undergo EDC/NHS chemistry with glycol-chitosan to form glycol-chitosan-coated MUA-QDs. Subsequent RGD ligand conjugation produces cRGDyk-GCM-QDs. (**ii**) NIR fluorescence images of an RR1022 tumor-bearing mouse, 24 hours after intravenous tail injection with cRGDyk-GCM-QDs. Top; supine position, bottom; prone position. Red indicates areas of highest fluorescence intensity. The red arrow indicates subcutaneous xenograft tumor location. Image adapted with permission from reference 12, copyright 2017 Springer Nature. **B**) (**i**) Schematic of InP/ZnSe/ZnS core/shell/shell QDs, showing the dual emission systems under a single excitation event. (**ii**) Maximum peak (PL) emission intensity spectra of InP core, InP/ZnSe core/shell, and InP/ZnSe/ZnS core/shell/shell QDs. (**iii**) Distribution of the PPA-based amphiphilic polymer wrapped InP/ZnSe/ZnS QDs, when intravenously injected into (top row) Bcl-7402 tumor-bearing mice, (middle row) MCF-7 tumor-bearing mice, and (bottom row) Bel-7402 tumor-bearing mice after 10 min, 1 hour, 4 hours, and 12 hours. Legend; (**i**) and (**ii**) rows were treated with PAA-based polymer-QDs surface modified with cRGD peptides; (**iii**) denotes mice treated with PAA-based polymer-QDs lacking the cRGD surface modification. The white circle indicates the location of the tumors within the mice. Image adapted with permission from reference 13, copyright 2017 The Royal Society of Chemistry. **C**) (**i**) Schematic of the synthesis of AIZS-GO nanocomposites from graphene oxide-oleylamine (GO-OAM). (**ii**) Cell viability of SK-BR-3 cells incubated with varying concentrations of AIZS-GO nanocomposites for 24 hours, as determined by MTT assay. (**iii**) *In vivo* fluorescence imaging of SK-BR-3 tumor-bearing mice intravenously injected with PBS (control) or 0.04 μg AIZS-GO nanocomposites. Image adapted with permission from reference 14, copyright 2017 Elsevier. **D**) (**i**) Schematic of loading mesoporous silica nanoparticles with Mn-doped ZnSe QDs to produce MSN@QDs. (**ii**) 4T1 cellular uptake efficiency of QDs, MSN@QDs, and TRF-MSN@QDs as determined by cellular fluorescence after 6 hours and 12 hours. (**iii**) Demonstration of *in vivo* imaging capabilities of s-QDs, MSN@QDs, and TRF-MSN@QDs delivered at the same concentration into a nude mouse bearing RR1022 rat fibrosarcoma cells via subcutaneous injection. s-QDs did not breach background fluorescence levels. Image adapted with permission from reference 15, copyright 2018 American Chemical Society.

transferrin ligand to make TRF-MSN@QDs. The group observed increased cellular uptake with the transferrin ligand in an *in vitro* 4T1 cell model as measured by cellular fluorescence intensity (**Figure 3Dii**). In a nude mouse, subcutaneous injections of single-QDs, MSN@QDs, and TRF-MSN@QDs were given, and the fluorescence was examined (**Figure 3Diii**). While single-QDs did not register above background fluorescence levels, MSN@QDs and TRF-MSN@QDs showed significant fluorescence intensity, suggesting that the enriching the QDs aided in bioimaging capability.

Critical Considerations, Toxicity, and Future Outlook

Recent significant advancements in developing non-Cd QDs for bioimaging and sensing show promise for alternative NP materials for biological applications. Still, challenges remain in terms of the long-term persistence of the core elemental components (e.g., In, Cu, Se). Just as with Cd-containing QDs, the potential leaching of metal ions from within the QD core is influenced by the physicochemical properties of the QDs, including size, shape, and surface ligand functionalization. These properties primarily determine the fate of the QDs' biodistribution, biodegradation, clearance, and elimination when administered *in vivo*. Currently, the primary technical challenge facing non-Cd QD development is focused on improved colloidal stability, biocompatibility, and targeting. Here, lessons learned from Cd QDs guide the engineering approach, but our current knowledge about the chemistry and synthetic parameters of non-Cd QDs impedes progress.

It is still challenging to make non-Cd QDs that rival the narrow PL bandwidth, high QY, and ease of spectral tuning (UV-NIR) available in the Cd QD series. It is an even further challenge to maintain these properties when the QDs are transferred to water. To date, the highest quality Cd QDs for use in biological applications are core/shell structures where a wider-band gap inorganic shell encapsulates the core and ideally prevents leaching of potentially toxic metal ions. ZnS shells are commonly used on Cd QDs to create a non-toxic outer surface, improve their PL, and increase their chemical and photostability. Additionally, biocompatible hydrophilic ligands and bioconjugation strategies have been optimized for ZnS coated QDs. Thus, non-Cd QDs should be amenable to incorporating a ZnS shell to transfer existing technology and ease their transition for replacing Cd-based QDs.

In particular, researchers have focused heavily on InP QDs as a less toxic alternative to Cd-based QDs. However, refinement of their properties via chemical synthesis is complicated by their covalent nature, available phosphorus precursors, sensitivity towards oxidation, and reaction mechanisms (nucleation and growth).[16] Bare InP QDs are notorious for being prone to oxidation while at the same time exhibiting poor QYs. It is, therefore, essential to overcoat them with passivating inorganic shells, such as ZnS, to enhance their PL efficiency and stability. Despite significant advances in synthesis and shell overcoat technology, it is still challenging to tune emission wavelengths and simultaneously yield bright samples with narrow line widths. Significant research effort is being made to refine the synthesis of InP QDs, understand their surface chemistry, and optimize their inorganic surface passivation. $CuInS_2$ QDs face many of these same challenges. Indeed, the origin of emission from $CuInS_2$ QDs is still being elucidated, making it even more challenging to achieve narrow PL from these QDs.[17] The formation of robust core/shell structures (e.g., $CuInS_2$/ZnS) is complicated by the rich surface chemistry of $CuInS_2$ QDs coupled with the influence of precursors and reaction conditions.[18] However, the successful formation of $CuInS_2$ QDs with stable ZnS shells enables more rapid testing of surface modifications, enhancing the potential for interfacing these QDs with biological systems.

Conclusion

Over time, the use of heavy metal-free QDs within biological applications has become more popular due to their notably reduced cytotoxicity. However, the challenge remains to develop a Cd-free QD with a narrow PL and concomitant high QY. While the core/shell model has been effective thus far when using heavy metal-free QDs in limited *in vivo* bioimaging work, these QDs still lag behind heavy metal-incorporating core/shell QDs in PL efficiency and QY. To combat this shortcoming, we expect to see further research on QD synthesis and use *in vitro*. We also expect to see further combinatorial approaches, including core/multi-shell structures and additional modifications post-QD synthesis. Looking forward, we anticipate approaches that utilize the QD's facilitation of bound ligands at its surface to enhance QD targeting ability for bioimaging use *in vivo*. Such technologies must leave the QD's imaging capabilities uncompromised while reliably directing the QD through the body to the desired imaging site. Finally, while the number of *in vivo* studies applying Cd-free QDs to bioimaging remains low compared to other approaches currently in the field of nanoscience, we believe more will emerge within the next several years.

Acknowledgments

The authors acknowledge the NRL Base Funding Program and the NRL Institute for Nanoscience for financial support. K.E.R. is a Ph.D. candidate in the Fischell Department of Bioengineering, University of Maryland College Park.

References

(1) Zhu, C. et al. *Pro. Nat. Sci. Mater.* **2019**, *29* (6), 628–640.
(2) Bradburne, C. E. et al. *Bioconjug. Chem.* **2013**, *24* (9), 1570–1583.
(3. Ye, L. et al. *Nat. Nanotechnol.* **2012**, *7* (7), 453–458.
(4) Yong, K.-T. et al. *Chem. Soc. Rev.* **2013**, *42* (3), 1236–1250.
(5) Hussain, S. et al. *Chem. Phys. Chem.* **2009**, *10* (9–10), 1466–1470.
(6) Bharali, D. J. et al. *J. Am. Chem. Soc.* **2005**, *127* (32), 11364–11371.
(7) Reiss, P. et al. *Small* **2009**, *5* (2), 154–168.
(8) Nemati, A. *Iran. J. Mater. Sci. Eng.* **2020**, *17* (2), 1–12.
(9) Brunetti, V. et al. *Nanoscale* **2013**, *5* (1), 307–317.
(10) Wu, Y.-Z. et al. *ACS Appl. Mater. Interfaces* **2017**, *9* (15), 13068–13078.
(11) Yang, Y. et al. *ACS Appl. Mater. Interfaces* **2017**, *9* (28), 23450–23457.
(12) Kim, E.-M. et al. *J. Nanopart. Res.* **2017**, *19* (7), 251.
(13) Zhang, J. et al. *J. Mater. Chem. B* **2017**, *5* (41), 8152–8160.
(14) Zang, Z. et al. *Sensor. Actuat. B-Chem.* **2017**, *252*, 1179–1186.
(15) Zhou, R. et al. *ACS Appl. Mater. Interfaces* **2018**, *10* (40), 34060–34067.
(16) Tamang, S.; Lincheneau, C.; Hermans, Y.; Jeong, S.; Reiss, P. *Chem. Mater.* **2016**, *28* (8), 2491–2506.
(17) Fuhr, A. S. et al. *ACS Photonics* **2017**, *4* (10), 2425–2435.
(18) Berends, A. C. et al. *Chem. Mater.* **2018**, *30* (7), 2400–2413.

CdS/ZnS Core-shell Type Quantum Dots

Form	Description	Fluorescence Emission, λem (nm)	Cat. No.
4 µM in PBS, dispersion	amine	450	**900304-250UL**
1 mg/mL in H_2O, dispersion	carboxylic acid	450	**900294-1ML**
lyophilized powder	carboxylic acid	400	**900310-1MG**
solid	carboxylic acid	425	**900308-1MG**
	carboxylic acid	450	**900332-1MG**
powder	oleic acid	425	**900283-10MG**
solid	oleic acid	450	**900282-10MG**
5 mg/mL in toluene, dispersion	oleic acid	450	**900334-1ML**
4 µM in H_2O, dispersion	PEG	450	**900301-250UL**

CdSe/ZnS Core-shell Type Quantum Dots

Form	Description	Fluorescence Emission, λ_{em} (nm)	Cat. No.
1 mg/mL in water	amine	450	**919535-1MG**
	amine	470	**919268-1MG**
	amine	500	**919276-1MG**
	amine	520	**919284-1MG**
	amine	540	**919292-1MG**
	amine	560	**919306-1MG**
	amine	580	**919314-1MG**
	amine	600	**919322-1MG**
	amine	620	**919330-1MG**
	amine	650	**919497-1MG**
	carboxylic acid	470	**918822-1MG**
	carboxylic acid	520	**918865-1MG**
	carboxylic acid	540	**918814-1MG**
	carboxylic acid	560	**919152-1MG**
	carboxylic acid	580	**919160-1MG**
	carboxylic acid	600	**919179-1MG**
	carboxylic acid	620	**919187-1MG**
	carboxylic acid	650	**919195-1MG**
5 mg/mL in toluene	oleic acid	470	**919039-10MG**
	oleic acid	500	**919047-10MG**
	oleic acid	520	**919055-10MG**
	oleic acid	540	**919063-10MG**
	oleic acid	560	**919071-10MG**
	oleic acid	650	**919136-10MG**
	oleic acid	580	**919209-10MG**
	oleic acid	600	**919217-10MG**
	oleic acid	620	**919225-10MG**
solid	stabilized with octadecylamine ligands	540	**748056-10MG** **748056-25MG**
	stabilized with octadecylamine ligands	560	**748080-10MG** **748080-25MG**
	stabilized with octadecylamine ligands	580	**748129-10MG** **748129-25MG**
	stabilized with octadecylamine ligands	600	**748099-10MG** **748099-25MG**
	stabilized with octadecylamine ligands	620	**790192-10MG** **790192-25MG**
	stabilized with octadecylamine ligands	630	**790206-10MG** **790206-25MG**
4 µM in 10 mM PBS	amine	520	**900229-250UL**
	amine	540	**900235-250UL**
	amine	560	**900236-250UL**
	amine	580	**900237-250UL**
	amine	600	**900238-250UL**
	amine	620	**900239-250UL**
	amine	645	**900241-250UL**
1 mg/mL in H_2O	carboxylic acid	520	**900248-1ML**
	carboxylic acid	540	**900221-1ML**
	carboxylic acid	560	**900225-1ML**
	carboxylic acid	580	**900222-1ML**
	carboxylic acid	600	**900223-1ML**
	carboxylic acid	620	**900224-1ML**
	carboxylic acid	645	**900226-1ML**
5 mg/mL in toluene	stabilized with octadecylamine ligands	520	**900214-1ML**
	stabilized with octadecylamine ligands	540	**900215-1ML**
	stabilized with octadecylamine ligands	560	**900216-1ML**
	stabilized with octadecylamine ligands	580	**900217-1ML**
	stabilized with octadecylamine ligands	600	**900218-1ML**
	stabilized with octadecylamine ligands	620	**900219-1ML**
	stabilized with octadecylamine ligands	645	**900250-1ML**
powder	stabilized with octadecylamine ligands	645	**900212-10MG**
solid	stabilized with octadecylamine ligands	665	**900213-10MG**

Form	Description	Fluorescence Emission, λ_{em} (nm)	Cat. No.
4 µM in H_2O, dispersion	PEG	520	**900243-250UL**
	PEG	580	**900246-250UL**
	PEG	620	**900247-250UL**
solid	stabilized with octadecylamine ligands	520	**748021-10MG** **748021-25MG**

Cd-based Core-shell Quantum Dots with Streptavidin

Form	Fluorescence Emission, λ_{em} (nm)	Cat. No.
1 µM	450	**OCNQSS450-0.5ML** **OCNQSS450-2ML**
	490	**OCNQSS490-0.5ML** **OCNQSS490-2ML**
	525	**OCNQSS525-0.5ML** **OCNQSS525-2ML**
	540	**OCNQSS540-0.5ML** **OCNQSS540-2ML**
	560	**OCNQSS560-0.5ML** **OCNQSS560-2ML**
	580	**OCNQSS580-0.5ML** **OCNQSS580-2ML**
	600	**OCNQSS600-0.5ML** **OCNQSS600-2ML**
	620	**OCNQSS620-0.5ML** **OCNQSS620-2ML**
	645	**OCNQSS645-0.5ML** **OCNQSS645-2ML**
	665	**OCNQSS665-0.5ML** **OCNQSS665-2ML**

EDC Conjugation Kits for Carboxylic Cd-based Core/Shell Quantum Dots

Description	Fluorescence Emission, λ_{em} (nm)	Cat. No.
for 4 conjugation	450	**OCNQCK450-1KT**
for 4 conjugation	490	**OCNQCK490-1KT**
for 4 conjugation	525	**OCNQCK525-1KT**
for 4 conjugation	540	**OCNQCK540-1KT**
for 4 conjugation	560	**OCNQCK560-1KT**
for 4 conjugation	580	**OCNQCK580-1KT**
for 4 conjugation	600	**OCNQCK600-1KT**
for 4 conjugation	620	**OCNQCK620-1KT**
for 4 conjugation	645	**OCNQCK645-1KT**
for 4 conjugation	665	**OCNQCK665-1KT**

SMCC Conjugation Kits for Amine Cd-based Core/Shell Quantum Dots

Description	Fluorescence Emission, λ_{em} (nm)	Cat. No.
for 4 conjugation	450	**OCNQAK450-1KT**
for 4 conjugation	490	**OCNQAK490-1KT**
for 4 conjugation	525	**OCNQAK525-1KT**
for 4 conjugation	540	**OCNQAK540-1KT**
for 4 conjugation	560	**OCNQAK560-1KT**
for 4 conjugation	580	**OCNQAK580-1KT**
for 4 conjugation	600	**OCNQAK600-1KT**
for 4 conjugation	620	**OCNQAK620-1KT**
for 4 conjugation	645	**OCNQAK645-1KT**
for 4 conjugation	665	**OCNQAK665-1KT**

Cadmium-free Quantum Dots

PbS

Form	Description	Fluorescence Emission, λ_{em} (nm)	Cat. No.
10 mg/mL in toluene	oleic acid coated	900	900733-5ML
	-	1000	900734-5ML
	oleic acid coated	1100	900735-5ML
	-	1200	900736-5ML
	oleic acid coated	1300	900737-5ML
	-	1400	900738-5ML
	oleic acid coated	1500	900728-5ML
	-	1600	900727-5ML

CsPb(Cl,Br)3-based Perovskite Quantum Dots

Form	Description	Fluorescence Emission, λ_{em} (nm)	Cat. No.
10 mg/mL in toluene	oleic acid and oleylamine coated	450	900748-5ML
	oleic acid and oleylamine coated	480	900747-5ML
	oleic acid and oleylamine coated	510	900746-5ML

InP/ZnS

Form	Description	Fluorescence Emission, λ_{em} (nm)	Cat. No.
5 mg/mL in toluene	stabilized with oleylamine ligands	530	776750-5ML
	stabilized with oleylamine ligands	560	776793-5ML
	stabilized with oleylamine ligands	590	776769-5ML
	stabilized with oleylamine ligands	620	776777-5ML
	stabilized with oleylamine ligands	650	776785-5ML

Advances of Noble Bimetallic Nanoparticles in Detection of Glucose Level




Catherine P. O'Connell*, Linh B. Truong*, Thomas J. Webster+, David Medina Cruz+

Department of Chemical Engineering, Northeastern University, Boston, MA 02115, USA
*These authors contributed the same to the article
+Email: davidmedinacrz@gmail.com, th.webster@neu.edu

Introduction

Diabetes mellitus is a disease characterized by insulin insufficiency, which causes spikes in blood glucose (hyperglycemia), or reduced glucose (hypoglycemia).[1] While Type 1 Diabetes is characterized by the lack of insulin production from birth, Type II, the most common form of diabetes, is related to the improper use of insulin in the body. Since diabetes is an incurable disease, many patients must learn to manage and treat it appropriately.

Controlling glucose levels is a critical step for successful management of diabetes.[1] Currently, blood-glucose concentration can be measured directly through a glucose biosensor or indirectly using a hydrogen peroxide (H_2O_2) biosensor. Glucose molecules break down into H_2O_2, which links the analysis of H_2O_2 to glucose concentration and presenting an orthogonal approach to glucose sensing.[2–4] However, blood-glucose monitoring can be an invasive process, requiring a portion of the instrument to pierce the skin. Furthermore, traditional glucose sensors depend on enzymatic activity, which relies on temperature, humidity, and interference. Therefore, their windows of effectiveness and accuracy are narrow.[5]

Thus, there is a need to develop new glucose monitoring methods that are less invasive and more reliable. Nanotechnology can offer several potential approaches to addressing this challenge. Monometallic nanoparticles (NPs) have improved surface characteristics and catalytic properties depending on the element used. However, they suffer from some limitations in terms of toxicity and physicochemical properties. Noble bimetallic nanoparticles (BMNPs) present an alternative that can achieve significant functionality enhancement by combining different metal elements — making BMNPs useful potential tools in blood-glucose biosensing with limited invasiveness and enzymatic dependence. Research shows BMNPs have improved the analytical performance of sensors concerning sensitivity and selectivity.[6]

Research has already demonstrated the application of gold (Au) and silver (Ag) NPs for use in glucose monitoring.[7] Au-based nanostructures exhibit the ability to oxidize glucose, making them ideal for measuring glucose concentration. Meanwhile, Ag-based structures exhibit the ability to induce an etching effect from the H_2O_2, making them ideal for measuring H_2O_2 concentration.[8] Combining these or other noble metals may provide an exciting alternative; as such, we discuss the current advances in noble BMNPs, specifically Au-based and Ag-based structures, and their glucose detection applications.

Ag-based Nanoparticles

Ag-based NPs, such as Ag-Au, Ag-Pt, and Ag-Pd NPs, exhibit exciting changes in their localized surface plasmon resonance (SPR), which help detect changes in H_2O_2 concentration.[9] Based on these characteristics, researchers can combine Ag with other metals to produce a stable, sensitive, enzyme-free biosensor for H_2O_2. For instance, Li et al. constructed a novel Ag-Au NPs alloy embedded into copper oxide (Cu_2O) nanocubes on reduced graphene oxide (RGO) nanosheets for H_2O_2 detection. The nanocomposite synthesis occurred in a two-step photo-reduction method, depositing the product onto RGO sheets. The structure showed suitable electrocatalytic activities in the presence of H_2O_2, with a linear range of 0.05–50.75 mmol/L (mM) at -0.2 V, a detection limit of 0.1 μM, and sensitivity of 0.14 μA $mM^{-1}cm^{-2}$. Moreover, the nanocomposite exhibited selectivity in the presence of interfering species, along with a fast response time concerning changes in H_2O_2 concentration, resetting a steady state after 2 seconds.[10]

Similarly, researchers used a green synthesis approach to fabricate Ag-Au NPs using alginate which were subsequently deposited onto a RGO surface. The resulting Ag-Au/RGO product was deposited onto a carbon electrode. The resulting sensor exhibited high stability and selectivity to H_2O_2 and demonstrated wide dynamic range and high sensitivity. Interestingly, the study showed that the reduction of H_2O_2 was limited by the diffusion rate, not the catalysis rate.[11] Sun et al. also utilized Ag-Au NPs performing *in situ* reductions by polydopamine (PDA) onto a carbon-fiber microelectrode. At optimal conditions at 20:80 Ag:Au atomic composition, the resulting electrode gave linear measurements over the range of 0–0.055 mM and 0.055–2.775 mM, with excellent sensitivity of 12966 μA $mM^{-1}cm^{-2}$ and 2534 μA $mM^{-1}cm^{-2}$, respectively. These results indicated that this sensor could potentially be suitable to detect trace amounts of H_2O_2.[12]

Other metal elements beyond Ag-Au NPs structures have also been utilized because of their synergistic effect. For instance, research shows platinum (Pt) can enhance the material's overall electrocatalytic activities.[13] In an interesting report, equimolar Ag-Pt NPs were synthesized, deposited onto the RGO surface, and coated on glassy carbon electrodes. This resulted in a wide linear range of measurement, high sensitivity, and a low detection limit. This performance was attributed to the synergistic combination of the RGO and Ag-Pt NPs. Samples of fetal bovine serum were tested using the Ag-Pt/RGO sensor, showing results within 5% of known concentration. Researchers also demonstrated glucose detection by measuring glucose oxidase presence.[14] Additionally, an alternative method of UV-assisted synthesis of Ag-Pt NPs/RGO nanocomposite was recently performed. Significantly, this structure exhibited enzyme-like kinetics, catalyzing 3,3′,5,5′-tetramethylbenzidine (TMB) in the presence of H_2O_2. The reaction produced a light blue color. Therefore, a colorimetric assay was used to determine the concentration of H_2O_2 instead of an electrochemical assay. At 652 nm absorbance, the assay exhibited a linear range of 0–1 mM, with the limit of detection of 0.9 μM. This work showed potential for a fast and portable strip test of H_2O_2 concentration.[15]

Like Pt, palladium (Pd) shows many advantageous properties, including its high electrocatalytic activity.[16] Guler et al. investigated its potential for H_2O_2 detection using carbon electrodes coated with Ag-Pd NPs/Naflon (NA) on RGO nanocomposites, where NA was used as a protective membrane to the electrode's surface. The RGO was functionalized with (3-aminopropyl) triethoxysilane (APTES) before exposure to Ag-Pd NPs/NA. Fourier-transform infrared spectroscopy (FTIR), X-ray diffraction (XRD), and Transmission electron microscopy (TEM) characterization confirmed the formation of the structure. Catalytic performance was tested through cyclic voltammetry, and the result indicated enhanced electrochemical activity of the Ag-Pt/NA electrode compared with only NA, Ag-NA, and Pt-NA electrodes, proving the synergistic effect of Ag and Pt. Samples of milk were analyzed to validate the sensor's applicability, and the H_2O_2 concentration was determined to be accurate, with deviations within 3% of the known values, suggesting the sensor's readiness for analysis of relevant samples.[17]

Overall, the detection of H_2O_2 using Ag-based BMNP structures presents a novel method that is both sensitive, stable, and enzyme independent. Measurement of H_2O_2 using Ag-based BMNPs can indicate the concentration of glucose as well as the enzyme's activity in the oxidation pathway — potentially providing more information than just glucose sensing.

Au-based Nanoparticles

Au-Pt NPs have been used frequently as catalysts in oxidation reactions since the noble metal synergy shows sound synergistic effects. For example, Pt can act as the leading site for a dehydrogenation reaction, and Au and Pt can synergistically facilitate oxidative desorption and CO adsorption.[18] These synergistic catalytic activities of Au-Pt NPs have been utilized recently in glucose sensors for diabetes.

For example, Shim et al. developed core-shell structured Au-Pt NPs with Au cores and Pt shells coated onto a carbon electrode (**Figure 1B–1C**). They were synthetically produced and purified by centrifugation, with additional Au incorporated in the nano-channels. The Au-Pt nanoshells showed improved sensitivity, stability, and selectivity. The fabricated sensor possessed desirable dynamic ranges and detection limits as listed in PBS saline solution at 0.35 V potential. No sensitivity data was reported, but a stability test indicated only a 5% deviation in measurement after 30 days at a pH of 7.5. Also, minimal interference effect from other bio-compounds was observed.[19] This result showed that Au-Pt sensors might exhibit resistance to other interfering molecules, thus, showing their selectivity.

Furthermore, Lin et al. synthesized a Au-Pt alloy using a hydrothermal reactor, loaded on nano-carbon carriers, and then modified onto glassy carbon electrodes. The result indicated that the optimal Au:Pt ratio for catalytic activity was 1:1. Stability testing was performed using 10mM glucose over an applied range of -0.6 to 0.6 volts for four days. After two days, the modified electrode maintained 95.4% of its initial current response, and after four days, the modified electrode maintained 84.5% of its initial response. Once the electrode was cleaned and analyzed between -0.5 V and 1.3 V with a newly fabricated electrode, the result was similar (**Figure 1D**).[20]

Doped electrodes are a novel approach for the design of AuPt NPs-enhanced sensors. To do this, researchers synthesized a boron-doped diamond electrode, and electrochemically deposited Au-Pt was the boron-doped diamond electrode's surface.[21] The sensor's optimal composition was observed at a 1:1 Au:Pt molar ratio, consistent with orthogonal studies. A stability study indicated 93% retention of initial current and observed high selectivity toward glucose; additionally, studies showed acceptable reproducibility with 3.2% reproducibility.

Primarily used to measure glucose concentration directly, Au-based bimetallic nanostructures also show versatility for H_2O_2 detection applications. Zhou et al. published research where Au-Pt NPs were electrodeposited onto molybdenum disulfide (MoS_2) nanoflowers for enzyme-free sensing of H_2O_2. The entire structure was then placed on a glassy carbon electrode. The

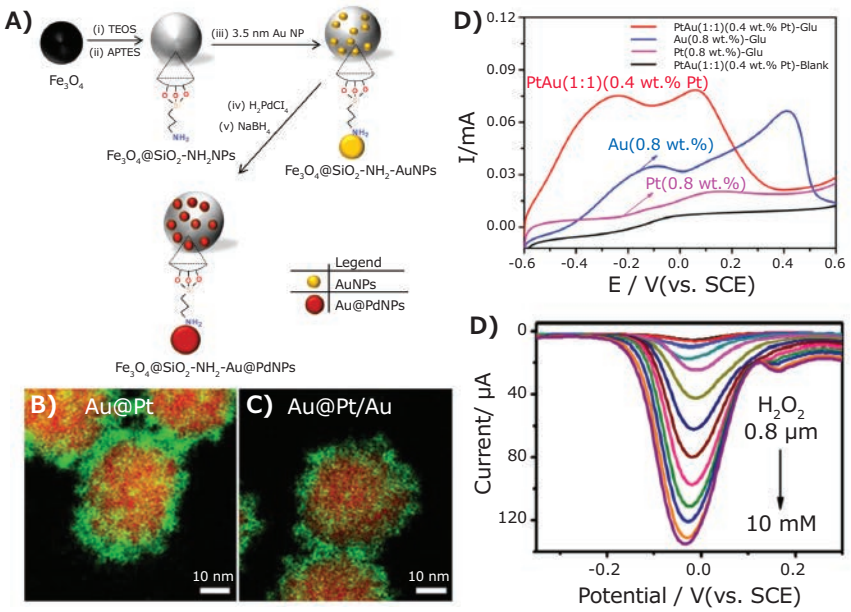

Figure 1. **A**) Schematic of the synthesis of Fe3O4@SiO2-NH2-Au@PdNPs. Reprinted with permission from reference 24, copyright 2020 American Chemical Society. **B**) High-angle annular dark-field scanning transmission electron microscope (HAADF-STEM) image of Au@Pt nanoparticles and **C**) of Au@Pt/Au nanoparticles. Reprinted with permission from reference 19, copyright 2019 Elsevier. **D**) Linear Sweep Voltammetry (LSV) of Pt/C, Au/C, and PtAu in 0.08M NaOH in the absence and presence of 10mM glucose. Reprinted with permission from reference 20, copyright 2020 Elsevier. **E**) Differential Pulse Voltammetry (DPV) responses of the Au-Pd/MoS2/GCE in H_2O_2 with different concentrations from 0.8µm to 10mM in Phosphate Buffered Saline (PBS) solution. Reprinted with permission from reference 25, copyright 2020 Elsevier.

AuPt-MoS_2 nanoflowers enhanced the electrode's performance. Like other Au-Pt structures, good stability was demonstrated (up to 20 days), with the response retaining 101.1% of the initial current response, while recording minimal interfering effects from other biomolecules.[22]

Because of its similar characteristics to Pt, Pd has also been used in conjunction with Au to substitute enzymatic biosensors in glucose monitoring. Au-Pd can enhance the catalytic activity of MoS_2 nanosheets because of the metal-metal interactions, promoting ion transfer to nanosheets, increasing the surface charge, and improving the affinity towards substrates.[23] Both factors contribute to the peroxidase-like activity of Au-Pd nanomaterials.

Andeniyi et al. developed nanomagnet-silica NPs decorated with Au-Pd. After synthesis of the magnetic NPs, Au-Pd was added via self-assembly. Interestingly, compared to horseradish-peroxidase, the peroxidase activity of the NPs was shown to be higher with a 70% increase in activity while following typical Michaelis-Menten enzyme kinetics, attributed to the synergistic interactions between Au and Pd. The addition of these nanostructures to a biosensor demonstrates improved selectivity, sensitivity, and stability compared to horse radish peroxidase — a known H_2O_2 catalysis (**Figure 1A**). Thus, these NPs have enhanced colorimetric biosensing ability for glucose detection.[24]

Furthermore, Li et al. synthesized MoS_2 nanosheets modified with Au-Pd NPs using a facile thermal co-reduction method, coated onto glassy carbon electrodes. Impressively, the resulting electrode acted as a bifunctional sensor for both glucose and H_2O_2. The synthesized non-enzymatic glucose sensor showed optimal linear response and sensitivity, as in the H_2O_2 application. Additionally, the modified electrode showed high selectivity to both H_2O_2 and glucose (**Figure 1E**). After 15 days, the electrode's performance indicated a 98% retention of the initial current response, providing strong stability. Determination of reproducibility for the five independent sensors found the RSD for glucose to be 8.2% and 7.5% for H_2O_2.[25]

The listed studies indicated the applicability and versatility of Au-based BMNPs in glucose detection. The resulting structures showed various ranges, thus offering customization to specific needs. Besides, the sensors remained selective toward glucose and stable in a biological environment.

A summary of current advances in Ag-based and Au-based noble bimetallic NP structure for glucose detection is found in **Table 1**.

Conclusion

There is a rising demand for an alternative, enzyme-free approach to monitoring glucose levels to manage diabetes. The catalytic activity, selectivity, and stability of BMNPs structures combined with the synergistic effects of different metal elements have the potential to provide more accurate and reliable glucose detection, both directly and by indirectly measuring H_2O_2. Here, we detailed various advances in the synthesis, characterization, and performance of Ag-based and Au-based BMNPs sensors. Overall, these structures provide flexibility in detection range, sensitivity, detection limits, and exhibit high selectivity and stability, properties that are highly sought after for helping diabetes patients monitor hypoglycemia and hyperglycemia episodes.

Table 1. Summary of Ag-based and Au-based Bimetallic NP Structure in Glucose Detection.

Bimetallic NPs-Modified Structure	Detected Molecules	Range (mM)	Detection Limit (μM)	Sensitivity (μA·mM^{-1}cm^{-2})	Ref
Ag-Au-Cu_2O on RGO	H_2O_2	0.05 – 50.75	0.1	0.14	10
Ag-Au on RGO	H_2O_2	0.1 – 10	0.57	112	11
Ag-Au/PDA	H_2O_2	0 – 0.055; 0.055 – 2.775	0.12	12966 2534	12
Ag-Pt on RGO	H_2O_2	0.005 – 1.5; 1.5 – 7.0	0.04	699.6 402.7	14
Ag-Pt on RGO	H_2O_2	0 – 1	0.9	Not Reported (NR)	15
Ag-Pd-NA on RGO	H_2O_2	0.002 – 19.5	0.7	1307	17
Au-Pt	Glucose	0.01 - 10	3	NR	20
Au-Pt	Glucose	0.0005 – 0.01 0.01 – 10	0.4457	NR	19
Au-Pt	Glucose	0.01 – 7.5	7.7	NR	21
Au-Pt-MoS2	H2O2	0.01 – 19.070	0.39	142.68	22
Au-Pd – $Fe_3O_4SiO_2$	Glucose	0.0001 – 0.06	0.06	NR	24
Au-Pd-MoS2	Glucose	0.5 – 20 0.0008 - 10	400 0.16	184.9	25

Nonetheless, despite promising results, *in vivo* experiments utilizing these modified electrodes still need to be performed. Therefore, future studies in the field should focus on validation in animals and ultimately to clinical translation. In the process, BMNPs have the potential to reduce invasiveness to the patient and improve device stability, two imperatives for diabetes management research and biosensing applications in general.

References

(1) Bruen, D.; Delaney, C.; Florea, L.; Diamond, D. *Sensors (Switzerland)* **2017**, *17* (8), 1–21. https://doi.org/10.3390/s17081866.

(2) Qin, X.; Lu, W.; Luo, Y.; Chang, G.; Asiri, A. M.; Al-Youbi, A. O.; Sun, X. *Anlst.* **2012**, *137* (4), 939–943. https://doi.org/10.1039/c2an15996a.

(3) Lin, L.; Song, X.; Chen, Y.; Rong, M.; Zhao, T.; Wang, Y.; Jiang, Y.; Chen, X. *Anal. Chim. Acta* **2015**, *869*, 89–95. https://doi.org/10.1016/j.aca.2015.02.024.

(4) Zong, C.; Wang, M.; Li, B.; Liu, X.; Zhao, W.; Zhang, Q.; Liang, A.; Yu, Y. *RSC Adv.* **2017**, *7* (43), 26559–26565. https://doi.org/10.1039/c7ra01498h.

(5) Shim, K.; Lee, W. C.; Heo, Y. U.; Shahabuddin, M.; Park, M. S.; Hossain, M. S. A.; Kim, J. H. *Sci. Rep.* **2019**, *9* (1), 1–7. https://doi.org/10.1038/s41598-018-36759-5.

(6) Mandal, R.; Baranwal, A.; Srivastava, A.; Chandra, P. *Biosens. Bioelectron.* **2018**, *117*, 546–561. https://doi.org/10.1016/j.bios.2018.06.039.

(7) Agasti, S. S.; Rana, S.; Park, M. H.; Kim, C. K.; You, C. C.; Rotello, V. M. *Adv. Drug Deliv. Rev.* **2010**, *62* (3), 316–328. https://doi.org/10.1016/j.addr.2009.11.004.

(8) Gao, Y.; Wu, Y.; Di, J. *Spectrochim. Acta A Mol. Biomol. Spectrosc.* **2017**, *173*, 207–212. https://doi.org/10.1016/j.saa.2016.09.023.

(9) Tashkhourian, J.; Hormozi-Nezhad, M. R.; Khodaveisi, J.; Dashti, R. A *Sensor. Actuat. B-Chem.* **2011**, *158* (1), 185–189. https://doi.org/10.1016/j.snb.2011.06.002.

(10) Li, D.; Meng, L.; Xiao, P.; Jiang, D.; Dang, S.; Chen, M. *J. Electroanal. Chem.* **2017**, *791*, 23–28. https://doi.org/10.1016/j.jelechem.2017.03.010.

(11) Zhao, L.; Wang, Y.; Zhao, X.; Deng, Y.; Li, Q.; Xia, Y. *Nanomaterials* **2018**, *8* (7), 507. https://doi.org/10.3390/nano8070507.

(12) Sun, W.; Cai, X.; Wang, Z.; Zhao, H.; Lan, M. *Microchem. J.* **2020**, *154*, 104595. https://doi.org/10.1016/j.microc.2020.104595.

(13) Siriviriyanun, A.; Imae, T. *Phys. Chem. Chem. Phys.* **2013**, *15* (14), 4921–4929. https://doi.org/10.1039/c3cp43636e.

(14) Zhang, C.; Zhang, Y.; Du, X.; Chen, Y.; Dong, W.; Han, B.; Chen, Q. *Talanta* **2016**, *159*, 280–286. https://doi.org/10.1016/j.talanta.2016.06.047.

(15) Yao, L.; Kong, F. Y.; Wang, Z. X.; Li, H. Y.; Zhang, R.; Fang, H. L.; Wang, W. *Microchim. Acta* **2020**, *187* (7). https://doi.org/10.1007/s00604-020-04350-3.

(16) Klinkova, A.; De Luna, P.; Sargent, E. H.; Kumacheva, E.; Cherepanov, P. V. *J. Mater. Chem. A* **2017**, *5* (23), 11582–11585. https://doi.org/10.1039/c7ta00902j.

(17) Guler, M.; Turkoglu, V.; Bulut, A.; Zahmakiran, M. *Electrochim. Acta* **2018**, *263*, 118–126. https://doi.org/10.1016/j.electacta.2018.01.048.

(18) Luo, J.; Njoki, P. N.; Lin, Y.; Mott, D.; Wang, L.; Zhong, C. J. *Langmuir* **2006**, *22* (6), 2892–2898. https://doi.org/10.1021/la0529557.

(19) Shim, K.; Lee, W. C.; Park, M. S.; Shahabuddin, M.; Yamauchi, Y.; Hossain, M. S. A.; Shim, Y. B.; Kim, J. H. *Sensor. Actuator. B-Chem.* **2019**, *278*, 88–96. https://doi.org/10.1016/j.snb.2018.09.048.

(20) Lin, L.; Weng, S.; Zheng, Y.; Liu, X.; Ying, S.; Chen, F.; You, D. *J. Electroanal. Chem.* **2020**, *865*, 114147. https://doi.org/10.1016/j.jelechem.2020.114147.

(21) Nantaphol, S.; Watanabe, T.; Nomura, N.; Siangproh, W.; Chailapakul, O.; Einaga, Y. *Biosens. Bioelectron.* **2017**, *98*, 76–82. https://doi.org/10.1016/j.bios.2017.06.034.

(22) Zhou, J.; Zhao, Y.; Bao, J.; Huo, D.; Fa, H.; Shen, X.; Hou, C. *Electrochim. Acta* **2017**, *250*, 152–158. https://doi.org/10.1016/j.electacta.2017.08.044.

(23) Liu, X.; Huang, D.; Lai, C.; Qin, L.; Zeng, G.; Xu, P.; Li, B.; Yi, H.; Zhang, M. *Small* **2019**, *15* (17). https://doi.org/10.1002/smll.201900133.

(24) Adeniyi, O.; Sicwetsha, S.; Mashazi, P. *ACS Appl. Mater. Interfaces* **2020**, *12* (2), 1973–1987. https://doi.org/10.1021/acsami.9b15123.

(25) Li, X.; Du, X. *Sensor. Actuat. B-Chem.* **2017**, *239*, 536–543. https://doi.org/10.1016/j.snb.2016.08.048.

Silver Nanospheres

Description	Concentration	Dimension	Cat. No.
λ_{max} 420 nm	1 mg/mL in water	avg. part. size 40 nm	**807575-1ML**
	1 mg/mL in water	avg. part. size 50 nm	**807583-1ML**
λ_{max} 496 nm	1.10 mg/mL in water	avg. part. size 60 nm	**809462-1ML**
λ_{max} 460 nm	1 mg/mL in water	avg. part. size 80 nm	**807567-1ML**
λ_{max} 490 nm	1 mg/mL in water	avg. part. size 100 nm	**807559-1ML**
λ_{max} 515 nm	1 mg/mL in water	avg. part. size 200 nm	**807540-1ML**
λ_{max} 430 nm	1 mg/mL in water	avg. part. size 60 nm	**807419-1ML**
λ_{max} 460 nm	1 mg/mL in water	avg. part. size 80 nm	**807427-1ML**
λ_{max} 490 nm	1 mg/mL in water	avg. part. size 100 nm	**807435-1ML**
λ_{max} 495 nm	1 mg/mL in water	avg. part. size 200 nm	**807443-1ML**
λ_{max} 420 nm	1 mg/mL in water	avg. part. size 50 nm	**807400-1ML**
λ_{max} 400 nm	0.02 mg/mL (in 2mM aqueous sodium citrate)	avg. part. size 30 nm	**796123-25ML**
λ_{max} 420 nm	0.02 mg/mL (in 2mM aqueous sodium citrate)	avg. part. size 50 nm	**796131-25ML**
λ_{max} 455 nm	0.02 mg/mL (in 2mM aqueous sodium citrate)	avg. part. size 80 nm	**796158-25ML**
λ_{max} 485 nm	0.02 mg/mL (in 2mM aqueous sodium citrate)	avg. part. size 200 nm	**796166-25ML**
λ_{max} 435 nm	0.02 mg/mL in water	avg. part. size 60 nm	**796425-25ML**
λ_{max} 470 nm	0.02 mg/mL in water	avg. part. size 80 nm	**796433-25ML**
λ_{max} 495 nm	0.02 mg/mL in water	avg. part. size 100 nm	**796441-25ML**
λ_{max} 500 nm	0.02 mg/mL in water	avg. part. size 200 nm	**796468-25ML**
λ_{max} 415 nm	0.02 mg/mL in water	avg. part. size 40 nm	**796204-25ML**
λ_{max} 420 nm	0.02 mg/mL in water	avg. part. size 50 nm	**796212-25ML**
λ_{max} 430 nm	0.02 mg/mL in water	avg. part. size 60 nm	**796220-25ML**
λ_{max} 470 nm	0.02 mg/mL in water	avg. part. size 80 nm	**796239-25ML**
λ_{max} 485 nm	0.02 mg/mL in water	avg. part. size 100 nm	**796247-25ML**
λ_{max} 490 nm	0.02 mg/mL in water	avg. part. size 200 nm	**796255-25ML**
λ_{max} 410 nm	0.02 mg/mL in water	avg. part. size 40 nm	**796301-25ML**
λ_{max} 420 nm	0.02 mg/mL in water	avg. part. size 50 nm	**796328-25ML**
λ_{max} 430 nm	0.02 mg/mL in water	avg. part. size 60 nm	**796336-25ML**
λ_{max} 470 nm	0.02 mg/mL in water	avg. part. size 80 nm	**796344-25ML**
λ_{max} 500 nm	0.02 mg/mL in water	avg. part. size 200 nm	**796360-25ML**
λ_{max} 395 nm	0.02 mg/mL in water	avg. part. size 20 nm	**795933-25ML**
PVP functionalized, λ_{max} 485 nm	0.02 mg/mL in water	avg. part. size 200 nm	**796026-25ML**
Econix PVP 40 kDa (Polymer)	dried	5 nm	**NCXSEPD5-50MG** **NCXSEPD5-150MG** **NCXSEPD5-500MG** **NCXSEPD5-1000MG**
	dried	25 nm	**NCXSEPD25-50MG** **NCXSEPD25-150MG** **NCXSEPD25-500MG** **NCXSEPD25-1000MG**
	dried	50 nm	**NCXSEPD50-50MG**
	dried	75 nm	**NCXSEPD75-50MG** **NCXSEPD75-150MG** **NCXSEPD75-500MG** **NCXSEPD75-1000MG**
	dried	110 nm	**NCXSEPD110-50MG** **NCXSEPD110-150MG** **NCXSEPD110-500MG** **NCXSEPD110-1000MG**

Description	Concentration	Dimension	Cat. No.
NanoXact PVP 40 kDa (Polymer)	dried	5 nm	**NCXAGPD5-1MG** **NCXAGPD5-5MG** **NCXAGPD5-10MG**
	dried	10 nm	**NCXAGPD10-1MG** **NCXAGPD10-5MG** **NCXAGPD10-10MG**
	dried	20 nm	**NCXAGPD20-1MG** **NCXAGPD20-5MG** **NCXAGPD20-10MG**
	dried	30 nm	**NCXAGPD30-1MG** **NCXAGPD30-5MG** **NCXAGPD30-10MG**
	dried	40 nm	**NCXAGPD40-1MG** **NCXAGPD40-5MG** **NCXAGPD40-10MG**
	dried	50 nm	**NCXAGPD50-1MG** **NCXAGPD50-5MG** **NCXAGPD50-10MG**
	dried	60 nm	**NCXAGPD60**
	dried	70 nm	**NCXAGPD70-1MG** **NCXAGPD70-5MG** **NCXAGPD70-10MG**
	dried	75 nm	**NCXAGPD75-1MG** **NCXAGPD75-5MG** **NCXAGPD75-10MG**
	dried	80 nm	**NCXAGPD80-1MG** **NCXAGPD80-5MG** **NCXAGPD80-10MG**
	dried	100 nm	**NCXAGPD100-1MG** **NCXAGPD100-5MG** **NCXAGPD100-10MG**
	dried	200 nm	**NCXAGPD200-1MG** **NCXAGPD200-5MG** **NCXAGPD200-10MG**
Econix PVP 40 kDa (Polymer)	5 mg/mL in water	5 nm	**NCXSEPE5-25ML** **NCXSEPE5-100ML** **NCXSEPE5-500ML**
	5 mg/mL in water	25 nm	**NCXSEPE25-25ML** **NCXSEPE25-100ML** **NCXSEPE25-500ML**
	5 mg/mL in water	50 nm	**NCXSEPE50-25ML** **NCXSEPE50-100ML** **NCXSEPE50-500ML**
	5 mg/mL in water	75 nm	**NCXSEPE75-25ML** **NCXSEPE75-100ML** **NCXSEPE75-500ML**
	5 mg/mL in water	110 nm	**NCXSEPE110-25ML** **NCXSEPE110-100ML** **NCXSEPE110-500ML**
Aminated / Cationic Silica NanoXact Silica-Shelled	1 mg/mL in ethanol	50 nm	**NCXAGAH50-1ML** **NCXAGAH50-5ML** **NCXAGAH50-10ML**
	1 mg/mL in ethanol	70 nm	**NCXAGAH70-1ML** **NCXAGAH70-5ML** **NCXAGAH70-10ML**
	1 mg/mL in ethanol	100 nm	**NCXAGAH100-1ML** **NCXAGAH100-5ML** **NCXAGAH100-10ML**
NanoXact Silica-Shelled Standard (Silanol)	1 mg/mL in ethanol	50 nm	**NCXAGSH50-1ML** **NCXAGSH50-5ML** **NCXAGSH50-10ML**
	1 mg/mL in ethanol	70 nm	**NCXAGSH70-1ML** **NCXAGSH70-5ML** **NCXAGSH70-10ML**
	1 mg/mL in ethanol	100 nm	**NCXAGSH100-1ML** **NCXAGSH100-5ML** **NCXAGSH100-10ML**

Silver Nanoparticle Dispersion

Description	Concentration	Dimension	Cat. No.
-	0.02 mg/mL in aqueous buffer	particle size 10 nm (TEM)	**730785-25ML**
	0.02 mg/mL in aqueous buffer	particle size 20 nm (TEM)	**730793-25ML**
	0.02 mg/mL in aqueous buffer	particle size 40 nm (TEM)	**730807-25ML**
	0.02 mg/mL in aqueous buffer	particle size 60 nm (TEM)	**730815-25ML**
	0.02 mg/mL in aqueous buffer	particle size 100 nm (TEM)	**730777-25ML**
	5 wt. % in ethylene glycol	<100 nm (particle size TEM)	**758329-5G** **758329-25G**
for printing on ITO and glass	50-60 wt. % in tetradecane	particle size ≤10 nm	**736511-25G** **736511-100G**
	30-35 wt. % in triethylene glycol monoethyl ether	particle size ≤50 nm	**736481-100G**
for printing on ITO films	30-35 wt. % in triethylene glycol monomethyl ether	particle size ≤50 nm	**736473-25G** **736473-100G**
for printing on plastic films	30-35 wt. % in triethylene glycol monomethyl ether	particle size ≤50 nm	**736465-25G** **736465-100G**
for printing on polyimide films	50-60 wt. % in tetradecane	particle size ≤10 nm	**736503-25G** **736503-100G**

Platinum Nanospheres

Description	Concentration	Dimension	Cat. No.
-	0.05 mg/mL (2 mM aqueous sodium citrate buffer)	diameter 5 nm	**916056-100ML** **916056-25ML**
	0.05 mg/mL (2 mM aqueous sodium citrate buffer)	diameter 30 nm	**916307-25ML** **916307-100ML**
citrate functionalized, 50 nm diameter, 0.05 mg/mL in 2 mM aqueous sodium citrate buffer	-	-	**915041-100ML** **915041-25ML**
-	0.05 mg/mL (4 mM aqueous sodium citrate buffer)	diameter 70 nm	**915300-25ML** **915300-100ML**

Applications of Metallic Nanoparticles in Bio-imaging and Molecular Spectroscopy




Jun Ando,[1] Kazuki Bando,[2] Kota Koike,[2,3] Katsumasa Fujita,[2,3,4*]

[1] RIKEN Cluster for Pioneering Research, 2-1 Hirosawa, Wako, Saitama 351-0198, Japan
[2] Department of Applied Physics, Osaka University, 2-1 Yamadaoka, Suita, Osaka 565-0871, Japan
[3] Advanced Photonics and Biosensing Open Innovation Laboratory, AIST-Osaka University, Osaka University, 2-1 Yamadaoka, Suita, Osaka 565-0871, Japan
[4] Institute for Open and Transdisciplinary Research Initiatives, Osaka University, 2-1 Yamadaoka, Suita, Osaka 565-0871, Japan
[*] E-mail: fujita@ap.eng.osaka-u.ac.jp

Introduction

Metallic nanoparticles have been attractive for imaging and spectroscopic analysis of biological samples because of their unique optical properties induced by localized plasmon resonance.[1] Metallic nanoparticles with a variety of different physical parameters such as size, shape, metal composition, and assembly (**Figure 1**)[2] can be synthesized for use in a wide range of biological applications. In particular, gold nanoparticles (AuNPs) are widely used as optical contrast agents for bioimaging since they posess several advantages such as strong light scattering properties at visible wavelengths without photobleaching, high chemical stability, and low toxicity for use in biological samples. Researchers have demonstrated high spatiotemporal resolution optical imaging of AuNP-labeled biomolecules and intracellular organelles.[3-5] In addition to their use as a contrast agent, metallic nanoparticles also work as probes for surface-enhanced Raman scattering (SERS) spectroscopy to analyze biological molecules and cells.[6] With SERS spectroscopy, information of the molecular species near the metal surface can be obtained with high sensitivity and high spatial confinement. This enables analysis of biological functions and phenomena, such as organelle transportation,[7] drug uptake,[8] and cell division.[9] Herein, we review recent progress on metallic nanoparticle applications for bio-imaging and molecular spectroscopy of biological systems.

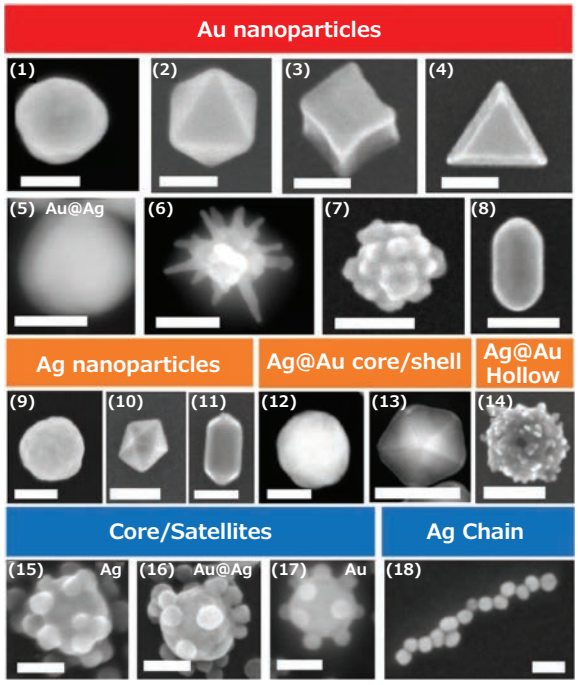

Figure 1. Electron microscope images of synthesized metallic nanoparticles with different shapes, sizes, metal compositions, and their assemblies. Scale bars: 50 nm. Reproduced with permission from reference 2, copyright 2019 American Chemical Society.

Tracking Biomolecules at Angstrom Precision and Microsecond Time Resolution

When labeled with AuNPs, the motions of biomolecules and intracellular organelles can be investigated by tracking the bright spot of the AuNP scattering image (**Figure 2A**). The localization precision of the optical image is inversely proportional to the square root of the photon number.[10] AuNPs provide a high scattering signal without photobleaching, allowing for nanometer-scale localization even at microsecond time resolution,[3,11] and AuNPs enable the analysis of the fast dynamics of biomolecules such as lipids and proteins.[4,12] To understand the working

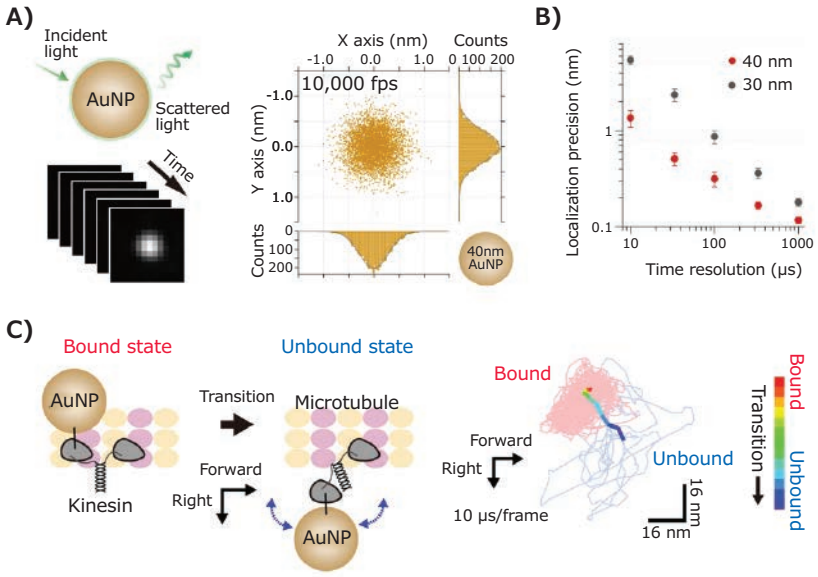

Figure 2. High-speed and high-precision tracking of kinesin labeled with a AuNP. **A**) Schematic showing dark-field imaging of a 40 nm AuNP, and 2D plots of a center positions of the AuNP images at 100 μs time resolution with an annular illumination total internal reflection dark-field microscope. **B**) A relationship between localization precisions and time resolutions with 40 nm and 30 nm AuNPs. **C**) Transition pathways from the microtubule-bound to microtubule-unbound state of a motor domain of kinesin-1 observed at 10 μs time resolution. **B** and **C** reproduced with permission from reference 13, copyright 2018 Elsevier.

mechanism of these tiny and complex biological molecules in detail, further improvements in localization precision are essential. Recently, researchers reported the development of an annular illumination total internal reflection dark-field microscope to illuminate AuNPs at high laser intensity.[13] The authors achieved a localization precision of 1.3 Å and 5.4 Å with 40 nm AuNPs at 1 ms and 33 μs time resolution (**Figure 2B**). This system revealed the fast stepping motions of kinesin-1 in detail, including a transition pathway of the motor domain from bound to unbound state on microtubule measured at a 10 μs time resolution (**Figure 2C**). Stepping motions of a processive chimeric dynein were also observed with a 30 nm AuNP at 100 μs time resolution, revealing 8 nm forward and backward steps and 5 nm side steps, consistent with the pitch of binding domains on the microtubule.[14] The use of small AuNPs as optical probes is crucial to minimize possible steric hindrances on the target biomolecules. Recently, the development of highly sensitive interferometric scattering microscopy achieved localized precision at a few nanometers with 20 nm AuNPs at microsecond time resolution.[4] Detection using smaller diameter AuNPs, such as 10 nm,[15] or even label-free direct detection of proteins,[16,17] has also been performed, expanding the range of measurable biomolecule types and phenomena.

Multicolor Imaging of Biomolecules with Ag, AgAu Alloy, and AuNPs

AuNP-based biomolecular tracking to date has been limited to monochromatic imaging. However, new methods have emerged that enable analysis of multiple biomolecules at high spatiotemporal resolution using additional color channels.

A multicolor high-speed single particle tracking system was recently developed using silver and silver-gold alloy nanoparticles (AgNPs and AgAuNPs) together with AuNPs (**Figure 3A**).[18] The peak wavelength of AgNPs in the extinction spectra is more than 100 nm shorter than that of AuNPs, and the AgAuNPs spectra are located between the AgNP and AuNP spectra and can be tuned depending on their composition ratio (**Figure 3B**).[19,20] To simultaneously observe each metal NP, a total internal reflection multicolor dark-field microscope was constructed with multiple lasers at 404 nm, 473 nm, and 561 nm that match the plasmon resonance wavelength of the AgNPs, AgAuNPs, and AuNPs, respectively. A spectrophotometer was used in the imaging optics to project scattering images at each wavelength on the different portions of a two-dimensional high-speed CMOS camera. With this system, multicolor imaging of phospholipid diffusional motions in a supported membrane (**Figure 3C–E**) and stepping motions of kinesin-1 along microtubules was achieved at 100 μs time resolution and nanometer-scale localization precision. This system also allows for the capture of the transient dimer formation of the two metal NPs, and a distance-dependent intensity increase in the 649 nm channel (**Figure 3F**). When two metal NPs are in sufficiently close proximity, plasmon coupling and a resulting redshift of the plasmon resonance wavelength are induced. The distance-dependent spectral shift has been used to create a highly accurate nano-ruler, known as a plasmon ruler, using two AuNPs or AgNPs and millisecond time resolution.[19] Multicolor imaging system extends the scope of the plasmon ruler with microsecond time resolution and multicolor imaging capabilities.

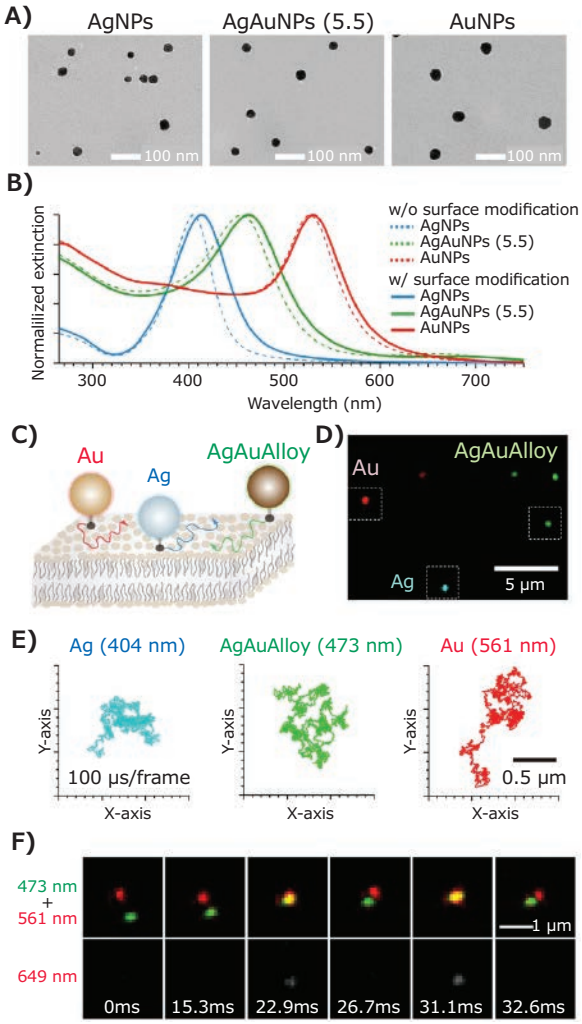

Figure 3. Multicolor high-speed tracking of phospholipids in a supported membrane. **A**) Electron microscope images of 30 nm AgNPs, 30 nm AgAuNPs, and 40 nm AuNPs. **B**) Extinction spectra of the AgNPs, AgAuNPs, and AuNPs without and with surface modification. **C**) Schematic illustration of phospholipids in a membrane, labeled with AuNPs, AgNPs, and AgAuNPs. **D**) Multicolor dark-field image of AgNPs, AgAuNPs, and AuNPs attached to phospholipids in a membrane with 404, 473, and 561 nm lasers. **E**) Trajectories of the center positions of the metal NPs, indicated by the white dotted rectangles in D, at 100 μs time resolution. **F**) Sequential dark-field images of AgAuNPs and AuNPs labeled phospholipids in the membrane during transient dimer formation, using a laser at 649 nm, for capturing plasmon coupling of two NPs. Reproduced with permission from reference 18, copyright 2019 American Chemical Society.)

Cell Imaging Using SERS: Drug Uptake and pH Sensing

Metallic nanoparticles are also widely used as SERS probes to amplify the Raman scattering signal from molecules near the metal surface, enabling highly sensitive Raman measurements of biomolecules, such as DNA, RNA, amino acids, proteins, and lipids.[6,21,22] Metallic nanoparticles introduced into cells work as SERS probes that report the molecular and chemical environment in cells near the metal surface.[23] Endocytosis is often used as a method of delivering metallic nanoparticles into cells. Culturing cells in a medium containing metallic nanoparticles allows the uptake by the cells; the nanoparticles eventually accumulate in endosomes and lysosomes through the intracellular transportation function.[23] The uptake of AuNPs into macrophage cells has been observed by slit-scanning Raman microscopy.[24,25] Time-resolved two-dimensional SERS images, captured at 2.5 minutes per frame, revealed the attachment of AuNPs on the cellular outer membranes and the entry into intracellular space. The analysis of SERS spectra obtained during time-lapse observations showed temporal fluctuation of the SERS signal and dependence of SERS spectra on the position of the AuNPs, indicating that the AuNPs report the variation of chemical environments during transportation.

The detection of extrinsic molecules such as drugs, introduced into cells is an important application of SERS. Indeed, SERS detection of anti-tumor and anti-leukemia drugs in cells has revealed much about drug distribution and metabolism in cells.[8,26,27] One of the difficulties of SERS-based drug detection has been its molecular specificity. SERS spectra from cells contain strong background signals from intrinsic molecules, and they often hinder the specific detection of target molecules. We have recently developed a SERS technique for drug imaging with high molecular specificity using an alkyne tag composed of a carbon-carbon triple bond.[28] Since the alkyne shows characteristic peaks in the Raman silent region of biomolecules from 1800 to 2600 cm^{-1}, alkyne-tagged molecules can be selectively detected without overlapping with intrinsic biomolecules.[29] Furthermore, the small chemical structure of the alkyne tag allows the drug molecule to essentially maintain its original properties, such as affinity to the drug target. Also, the high affinity of alkyne to metallic nanoparticles improves SERS detection sensitivity of both electromagnetic and chemical enhancement effects.[30-32] As a proof of concept, we used an alkyne-tagged inhibitor for cathepsin B, a drug target of tumor metastasis and localized in lysosomes. AuNPs were introduced into lysosomes in macrophage cells via endocytosis, and the alkyne-tagged inhibitor was subsequently administrated to the cell culture media at a concentration of 20 μM. When we performed time-lapse 3D SERS imaging of drug-treated cells with slit-scanning Raman microscopy, a gradual increase of the intensity of alkyne-SERS peak at 1980 cm^{-1} was observed at around 10 minutes after drug administration (**Figure 4**). The uptake speed of the inhibitor was quantitatively evaluated by counting the number of alkyne-SERS signals. Alkyne-tag SERS microscopy opens new avenues for quantitative analysis of drug dynamics in living cells.

SERS with metallic nanoparticles also works as a sensing method for intracellular environments, such as pH[33-35] and redox potential.[36] For this purpose, the nanoparticle surface is functionalized with molecules that show a structural change depending on the surrounding environment. In particular, SERS-based pH sensing of cells has been widely investigated,[33-35] since pH value is related to various biological processes such as proliferation, apoptosis, and ion transport.[37] Improvement of SERS sensitivity results in fast pH measurement, providing

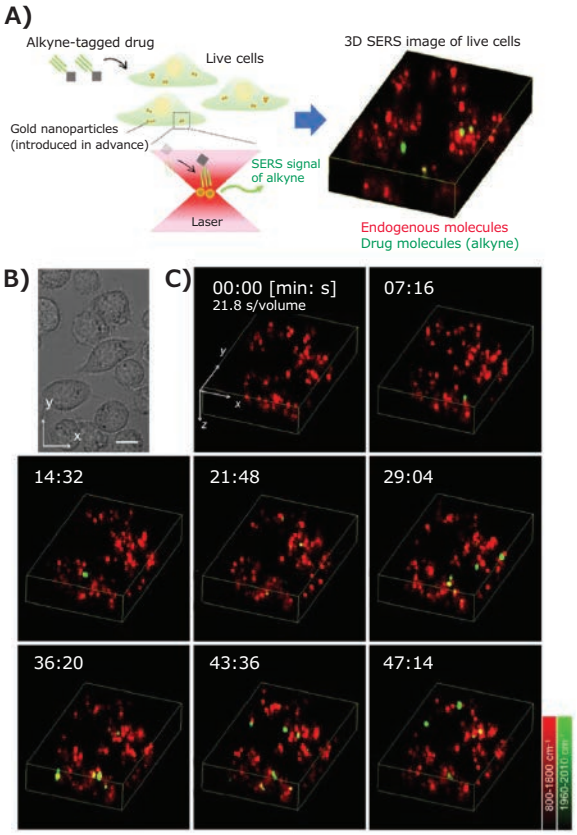

Figure 4. Uptake of small molecule drug into cells monitored by time-resolved alkyne-tag SERS microscopy. **A**) Schematic illustration of SERS detection of the alkyne-tagged small molecule drugs in living cells. **B**) A bright-field image of living macrophage cells cultured with 50 nm AuNPs. Scale bar = 10 μm. **C**) Three-dimensional SERS images of the same cells at different incubation times with alkyne-tagged cathepsin inhibitor. The inhibitor was administrated into the cell culture media at a concentration of 20 μM. The red color represents average Raman intensity from 800 to 1800 cm^{-1}. The green color represents the average Raman intensity from 1960 to 2010 cm^{-1}, which shows the existence of the alkyne-tagged inhibitor. Timelines indicate the incubation time after drug administration. The imaging volume was 50 × 82 × 15 μm. Reproduced with permission from reference 28, copyright 2020 American Chemical Society.

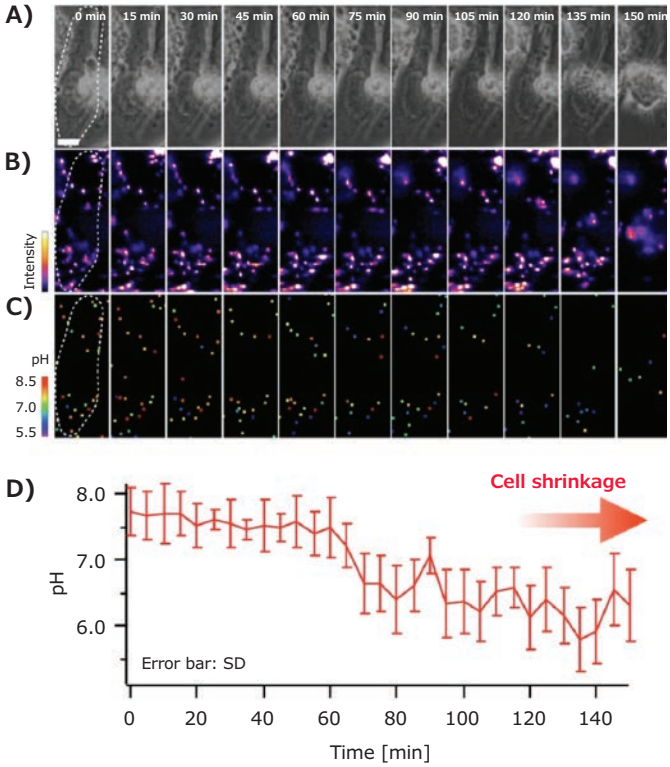

Figure 5. Time-lapse pH measurement of apoptotic cells with SERS. **A**) Phase contrast image of HeLa cells during apoptosis, induced by drug treatment. **B**) Two-dimensional distribution of the SERS intensity at 1590 cm^{-1}, assigned to benzene ring breathing mode of p-MBA attached on the metal nanoparticles. **C**) Local pH map of the intracellular space of a HeLa cell. The images show every 15 minutes/frame and the scale bar shows 10 μm. **D**) Plots of pH values over incubation time. Reproduced with permission from reference 2, copyright 2019 American Chemical Society.

a better understanding of the biological processes governed by dynamic pH changes. To identify the most sensitive metal nanoparticles for pH sensing, we synthesized 18 types of AuNPs and AgNPs (**Figure 1**), with different shapes, sizes, metal compositions, and assemblies. By evaluating the SERS activity, it was confirmed that Ag chain, Ag core/satellites, Ag@Au core/satellites, and Au core/satellites produced the strongest SERS signal, and that this signal is sufficient to perform pH sensing at the single-particle level. With Ag@Au core/satellites as SERS probe, changes in intracellular pH over time during the apoptotic process of HeLa cells was successfully revealed at a temporal resolution of 5 minutes (**Figure 5**).

Dynamic SERS tracking in a Living Cell

In recent years, particle tracking and SERS spectroscopy have been combined to perform dynamic SERS imaging inside biological cells.[7,25] Since endocytosed AuNPs travel around the intracellular space due to a cellular transportation function, intracellular molecules near the nanoparticle surface can be detected with a high spatiotemporal resolution by tracking the motion of AuNPs and performing SERS spectroscopy at the same time. This allows us to investigate the mechanisms of various biomolecules involved in cellular transportation. For this purpose, a laser-scanning Raman microscope and a dark-field microscope were combined to acquire SERS signal from a specific nanoparticle in a cell continuously.[7,25] Information on particle positions is obtained by dark-field microscopy and used to continuously relocate the focus position of Raman excitation laser on the same nanoparticle. The temporal resolution of this SERS tracking system was 50 ms per spectrum. SERS measurements were performed on macrophage cells with 50 nm AuNPs. During SERS measurement, motion-dependent changes in the SERS spectra were observed, indicating that the AuNPs report local molecular environment during transportation. Furthermore, using a dual-focus dark-field imaging system, the 3D SERS tracking technique has been developed, with which AuNPs that move three-dimensionally can be followed.[38] Recently, the 3D SERS tracking system was applied to local pH measurement inside cells (**Figure 6A**).[39] The nanoparticles, functionalized with pH-sensitive molecules, are thought to be transported to endosomes and lysosomes by intracellular trafficking after being taken up into cells by endocytosis. In general, during these trafficking pathways, the

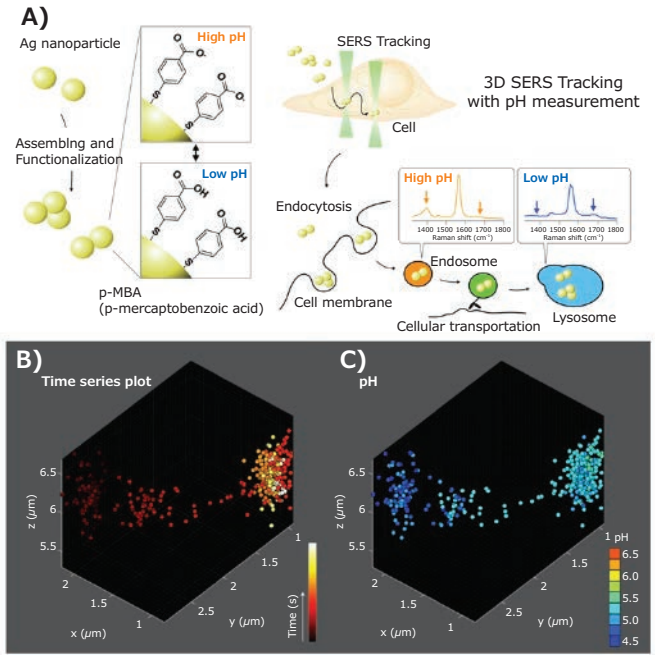

Figure 6. Dynamic pH measurement of intracellular pathways by SERS tracking. A) Schematic image of the intracellular pH measurement with surface-functionalized Ag nano-assemblies and 3D SERS tracking technique. B) Three-dimensional nanoparticle trajectory during intracellular transportation in a living HeLa cell at time resolution of 200 ms. The color scale represents the time course of the trajectory. C) pH changes during the intracellular transportation in a HeLa cell displayed on the 3D nanoparticle trajectory. pH value was obtained by the SERS intensity ratio of COO^- to C=O. Reproduced with permission from reference 39, copyright 2020 The Royal Society of Chemistry.

pH is gradually reduced from pH 6.3 in early endosomes to pH 5.5 in lysosomes.[40] Multi-modal imaging with SERS tracking and fluorescence imaging using lysosome-specific dye revealed that the pH value quantified by SERS analysis was low when the nanoparticles exist in lysosomes (**Figure 6B and C**).

Conclusion

In this manuscript, we discussed the recent progress on the applications of metallic nanoparticles for imaging and spectroscopy of biological systems. For bio-imaging, multicolor, high-speed and high-precision tracking of target molecules was demonstrated, and dynamic motions of biomolecules were investigated. For spectroscopic analysis with metal nanoparticles, SERS microscopy applications for drug uptake and pH sensing were summarized. Finally, we introduced an approach to combine particle tracking and SERS spectroscopy to analyze the intracellular molecular environment during transportation at high spatiotemporal resolution. These new metallic nanoparticle-based approaches for bio-imaging and molecular spectroscopy will further contribute to a wide range of research fields such as biology, drug development, and medical science in the future.

Acknowledgments

This work was partially supported by the grant of AMED-CREST under Grant JP18gm071000 and the Grants-in-Aid for Scientific Research (grant numbers JP18H01904 to JA) from the Ministry of Education, Culture, Sports, Science, and Technology of Japan.

References

(1) Anker, J. N.; Hall, W. P.; Lyandres, O.; Shah, N. C.; Zhao, J.; Van Duyne, R. P. *Nat Mater.* **2008**, *7* (6), 442–453.
(2) Zhang, Z.; Bando, K.; Mochizuki, K.; Taguchi, A.; Fujita, K.; Kawata, S. *Anal. Chem.* **2019**, *91* (5), 3254–3262.
(3) Nan, X.; Sims, P. A.; Xie, X. S. *Chem. Phys. Chem.* **2008**, *9* (5), 707–712.
(4) Lin, Y.-H.; Chang, W.-L.; Hsieh, C.-L. *Opt. Express* **2014**, *22* (8), 9159–9170.
(5) Iino, R.; Iida, T.; Nakamura, A.; Saita, E.-i.; You, H.; Sako, Y. *BBA-Gen. Subjects* **2018**, *1862* (2), 241–252.
(6) Ando, J.; Yano, T.-a.; Fujita, K.; Kawata, S. *Phys. Chem. Chem. Phys.* **2013**, *15* (33), 13713–13722.
(7) Ando, J.; Fujita, K.; Smith, N. I.; Kawata, S. *Nano Lett.* **2011**, *11* (12), 5344–5348.
(8) Yang, J.; Cui, Y.; Zong, S.; Zhang, R.; Song, C.; Wang, Z. *Mol. Pharm.* **2012**, *9* (4), 842–849.
(9) Kang, B.; Austin, L. A.; El-Sayed, M. A. *Nano Lett.* **2012**, *12* (10), 5369–5375.
(10) Thompson, R. E.; Larson, D. R.; Webb, W. W. *Biophys. J.* **2002**, *82* (5), 2775–2783.
(11) Ueno, H.; Nishikawa, S.; Iino, R.; Tabata, K. V.; Sakakihara, S.; Yanagida, T.; Noji, H. *Biophys. J.* **2010**, *98* (9), 2014–2023.
(12) Nakamura, A.; Okazaki, K.-i.; Furuta, T.; Sakurai, M.; Iino, R. *Nat. Commun.* **2018**, *9* (1), 3814–12.
(13) Ando, J.; Nakamura, A.; Visootsat, A.; Yamamoto, M.; Song, C.; Murata, K.; Iino, R. *Biophys. J.* **2018**, *115* (12), 2413–2427.
(14) Ando, J.; Shima, T.; Kanazawa, R.; Shimo-Kon, R.; Nakamura, A.; Yamamoto, M.; Kon, T.; Iino, R. *Sci. Rep.* **2020**, *10* (1), 1080.
(15) Liao, Y.-H.; Lin, C.-H.; Cheng, C.-Y.; Wong, W. C.; Juo, J.-Y.; Hsieh, C.-L. *ACS Nano* **2019**, *13* (10), 10918–10928.
(16) Ortega Arroyo, J.; Andrecka, J.; Spillane, K. M.; Billington, N.; Takagi, Y.; Sellers, J. R.; Kukura, P. *Nano Lett.* **2014**, *14* (4), 2065–2070.
(17) Piliarik, M.; Sandoghdar, V. *Nat. Commun.* **2014**, *5*, 4495.
(18) Ando, J.; Nakamura, A.; Yamamoto, M.; Song, C.; Murata, K.; Iino, R. *ACS Photonics* **2019**, *6* (11), 2870–2883.
(19) Sönnichsen, C.; Reinhard, B. M.; Liphardt, J.; Alivisatos, A. P. *Nat. Biotechnol.* **2005**, *23* (6), 741–745.
(20) Link, S.; Wang, Z. L.; El-Sayed, M. A. *J. Phys. Chem. B* **1999**, *103* (18), 3529–3533.
(21) Liu, M.; Li, Q.; Liang, L.; Li, J.; Wang, K.; Li, J.; Lv, M.; Chen, N.; Song, H.; Lee, J.; Shi, J.; Wang, L.; Lal, R.; Fan, C. *Nat. Commun.* **2017**, *8* (1), 3375.
(22) Shiota, M.; Naya, M.; Yamamoto, T.; Hishiki, T.; Tani, T.; Takahashi, H.; Kubo, A.; Koike, D.; Itoh, M.; Ohmura, M.; Kabe, Y.; Sugiura, Y.; Hiraoka, N.; Morikawa, T.; Takubo, K.; Suina, K.; Nagashima, H.; Sampetrean, O.; Nagano, O.; Saya, H.; Yamazoe, S.; Watanabe, H.; Suematsu, M. *Nat. Commun.* **2018**, *9* (1), 1561.
(23) Kneipp, J.; Kneipp, H.; McLaughlin, M.; Brown, D.; Kneipp, K. *Nano Lett.* **2006**, *6* (10), 2225–2231.
(24) Fujita, K.; Ishitobi, S.; Hamada, K.; Smith, N. I.; Taguchi, A.; Inouye, Y.; Kawata, S. *J. Biomed. Opt.* **2009**, *14* (2), 024038.
(25) Palonpon, A. F.; Ando, J.; Yamakoshi, H.; Dodo, K.; Sodeoka, M.; Kawata, S.; Fujita, K. *Nat. Protoc.* **2013**, *8* (4), 677–692.
(26) Chourpa, I.; Morjani, H.; Riou, J. F.; Manfait, M. *FEBS Letters* **1996**, *397* (1), 61–64.
(27) Nabiev, I. R.; Morjani, H.; Manfait, M. *Eur. Biophys. J.* **1991**, *19* (6), 311–316.
(28) Koike, K.; Bando, K.; Ando, J.; Yamakoshi, H.; Terayama, N.; Dodo, K.; Smith, N. I.; Sodeoka, M.; Fujita, K. *ACS Nano* **2020**, *14* (11), 15032–15041.
(29) Yamakoshi, H.; Dodo, K.; Palonpon, A.; Ando, J.; Fujita, K.; Kawata, S.; Sodeoka, M. *J. Am. Chem. Soc.* **2012**, *134* (51), 20681–20689.
(30) Ando, J.; Asanuma, M.; Dodo, K.; Yamakoshi, H.; Kawata, S.; Fujita, K.; Sodeoka, M. *J. Am. Chem. Soc.* **2016**, *138* (42), 13901–13910.
(31) Ardini, M.; Huang, J.-A.; Sánchez, C. S.; Mousavi, M. Z.; Caprettini, V.; Maccaferri, N.; Melle, G.; Bruno, G.; Pasquale, L.; Garoli, D.; De Angelis, F. *Sci. Rep.* **2018**, *8* (1), 15910.
(32) Li, M.; Wu, J.; Ma, M.; Feng, Z.; Mi, Z.; Rong, P.; Liu, D. *Nanotheranostics* **2019**, *3* (1), 113–119.
(33) Talley, C. E.; Jusinski, L.; Hollars, C. W.; Lane, S. M.; Huser, T. *Anal. Chem.* **2004**, *76* (23), 7064–7068.
(34) Jaworska, A.; Jamieson, L. E.; Malek, K.; Campbell, C. J.; Choo, J.; Chlopicki, S.; Baranska, M. *Analyst* **2015**, *140* (7), 2321–2329.
(35) Kneipp, J.; Kneipp, H.; Wittig, B.; Kneipp, K. *Nano Lett.* **2007**, *7* (9), 2819–2823.
(36) Auchinvole, C. A. R.; Richardson, P.; McGuinnes, C.; Mallikarjun, V.; Donaldson, K.; McNab, H.; Campbell, C. J. *ACS Nano* **2012**, *6* (1), 888–896.
(37) Furuya, Y.; Lundmo, P.; Short, A. D.; Gill, D. L.; Isaacs, J. T. *Cancer Res.* **1994**, *54* (23), 6167–6175.
(38) Huang, K.-C.; Bando, K.; Ando, J.; Smith, N. I.; Fujita, K.; Kawata, S. *Methods* **2014**, *68* (2), 348–353.
(39) Bando, K.; Zhang, Z.; Graham, D.; Faulds, K.; Fujita, K.; Kawata, S. *Analyst* **2020**, *145* (17), 5768–5775.
(40) Casey, J. R.; Grinstein, S.; Orlowski, J. *Nat. Rev. Mol. Cell Biol.* **2010**, *11* (1), 50–61.

Gold Nanoshells

Name	Absorption	Concentration (mg/mL)	Cat. No.
Bioready Carboxyl for Covalent Conjugation	-	in Water	**NCXGSXR150-5ML** **NCXGSXR150-30ML** **NCXGSXR150-100M**
Carboxyl (Lipoic Acid) NanoXact	660 nm	0.05 in water	**NCXGSLN660-25ML** **NCXGSLN660-100ML** **NCXGSLN660-500ML**
	800 nm	0.05 in water	**NCXGSLN800-25ML** **NCXGSLN800-100ML** **NCXGSLN800-500ML**
	980 nm	0.05 in water	**NCXGSLN980-25ML** **NCXGSLN980-100ML** **NCXGSLN980-500ML**
	660 nm	1 in water	**NCXGSLH660-500UL** **NCXGSLH660-1ML** **NCXGSLH660-5ML**
	800 nm	1 in water	**NCXGSLH800-500UL** **NCXGSLH800-1ML** **NCXGSLH800-5ML**
	980 nm	1 in water	**NCXGSLH980-500UL** **NCXGSLH980-1ML** **NCXGSLH980-5ML**
NanoXact mPEG 5 kDa (Polymer)	660 nm	0.05 in water	**NCXGSGN660-25ML** **NCXGSGN660-100ML** **NCXGSGN660-500ML**
	800 nm	0.05 in water	**NCXGSGN800-25ML** **NCXGSGN800-100ML** **NCXGSGN800-500ML**
	980 nm	0.05 in water	**NCXGSGN980-25ML** **NCXGSGN980-100ML** **NCXGSGN980-500ML**
	660 nm	1 in water	**NCXGSGH660-500UL** **NCXGSGH660-1ML** **NCXGSGH660-5ML**
	800 nm	1 in water	**NCXGSGH800-500UL** **NCXGSGH800-1ML** **NCXGSGH800-5ML**
	980 nm	1 in water	**NCXGSGH980-500UL** **NCXGSGH980-1ML** **NCXGSGH980-5ML**
NanoXact PVP 40 kDa (Polymer)	660 nm	0.05 in water	**NCXGSPN660-25ML** **NCXGSPN660-100ML** **NCXGSPN660-500ML**
	800 nm	0.05 in water	**NCXGSPN800-25ML** **NCXGSPN800-100ML** **NCXGSPN800-500ML**
	980 nm	0.05 in water	**NCXGSPN980-25ML** **NCXGSPN980-100ML** **NCXGSPN980-500ML**
	660 nm	1 in water	**NCXGSPH660-500UL** **NCXGSPH660-1ML** **NCXGSPH660-5ML**
	800 nm	1 in water	**NCXGSPH800-500UL** **NCXGSPH800-1ML** **NCXGSPH800-5ML**
	980 nm	1 in water	**NCXGSPH980-500UL** **NCXGSPH980-1ML** **NCXGSPH980-5ML**
Bioready Streptavidin	-	in aqueous conjugate buffer	**NCXGSIR150-200UL** **NCXGSIR150-1ML** **NCXGSIR150-5ML** **NCXGSIR150-10ML**

Gold Nanoparticles & Nanostructures

Non-surface Functionalized Nanoparticles & Nanostructures

Gold Nanoparticles

Description	Particle Size (nm)	Absorption	Concentration	Cat. No.
reactant free stabilized suspension in 0.1 mM PBS	5	510-525 nm	~ 5.5E+13 particles/mL	**752568-25ML 752568-100ML**
	10	510-525 nm	~ 6.0E+12 particles/mL	**752584-25ML 752584-100ML**
	20	518-522 nm	~ 6.54E+11 particles/mL	**753610-25ML 753610-100ML**
	30	524-527 nm	~ 1.8E+11 particles/mL	**753629-25ML 753629-100ML**
	50	535-536 nm	~ 3.5E+10 particles/mL	**753645-25ML 753645-100ML**
	80	550-557 nm	~ 7.8E+9 particles/mL	**753661-25ML 753661-100ML**
	100	564-574 nm	~ 3.8E+9 particles/mL	**753688-25ML 753688-100ML**
	40	529-533 nm	~ 7.2E+10 particles/mL	**753637-25ML 753637-100ML**
	60	538-544 nm	~ 1.9E+10 particles/mL	**753653-25ML 753653-100ML**
	15	510-520 nm	~ 1.64E+12 particles/mL	**777099-25ML 777099-100ML**
	400	-	~ 1.9E+8 particles/mL	**746681-25ML**
stabilized suspension in citrate buffer	5	510-525 nm	~ 5.5E+13 particles/mL	**741949-25ML 741949-100ML**
	10	510-525 nm	~ 6.0E+12 particles/mL	**741957-25ML 741957-100ML**
	15	510-525 nm	~ 1.64E+12 particles/mL	**777137-25ML 777137-100ML**
	20	518-522 nm	~ 6.54E+11 particles/mL	**741965-25ML 741965-100ML**
	30	524-527 nm	~ 1.8E+11 particles/mL	**741973-25ML 741973-100ML**
	80	551-557 nm	~ 7.8E+9 particles/mL	**742023-25ML 742023-100ML**
	40	529-533 nm	~ 7.2E+10 particles/mL	**741981-25ML 741981-100ML**
	100	564-574 nm	~ 3.8E+9 particles/mL	**742031-25ML 742031-100ML**
	50	533-536 nm	~ 3.5E+10 particles/mL	**742007-25ML 742007-100ML**
	150	-	~ 3.6E+9 particles/mL	**742058-25ML 742058-100ML**
	60	538-544 nm	~ 1.9E+10 particles/mL	**742015-25ML 742015-100ML**
	200	-	~ 1.9E+9 particles/mL	**742066-25ML 742066-100ML**
	250	-	~ 7.1E+8 particles/mL	**742074-25ML 742074-100ML**
	300	-	~ 4.5E+8 particles/mL	**742082-25ML**
	400	-	~ 1.9E+8 particles/mL	**742090-25ML**
dispersion in H_2O silica coated	10	514-524 nm	~ 7.1E+12 particles/mL	**747564-5ML**
	20	518-528 nm	~ 8.5E+11 particles/mL	**747572-5ML**
	5	-	~ 6.6E+13 particles/mL	**747556-5ML**

Gold Nanorods

Particle Size (nm)	Absorption	Concentration (µg/mL)	Cat. No.
10	808 nm	> 30 in H_2O	**716820-25ML**
	850 nm	> 30 in H_2O	**716839-25ML**
25	650 nm	> 45 in H_2O	**771686-25ML**
	600 nm	> 45 in H_2O	**771651-25ML**
	550 nm	> 45 in H_2O	**771643-25ML**
10	980 nm	> 30 in H_2O	**776661-25ML**
	900 nm	≥ 30 in H_2O	**776653-25ML**
	980 nm	> 30 in H_2O	**776688-25ML**
	808 nm	> 30 in H_2O	**747998-5ML**
	850 nm	> 30 in H_2O	**748005-5ML**
	780 nm	> 30 in H_2O	**747971-5ML**

Particle Size (nm)	Absorption	Concentration (µg/mL)	Cat. No.
25	650 nm	50 in H_2O	**900367-25ML**
	550 nm	50 in H_2O	**900366-25ML**
10	1064 nm	35 in H_2O	**900365-25ML**
	980 nm	35 in H_2O	**900364-25ML**
	808 nm	35 in H_2O	**900363-25ML**
	780 nm	35 in H_2O	**900362-25ML**
	780 nm	> 30 in H_2O	**716812-25ML**

Gold Nanospheres

Description	Particle Size (nm)	Cat. No.
Bare Bioready for Passive Adsorption in Aqueous Sodium Citrate	40	**NCXAUCR40-5ML** **NCXAUCR40-30ML** **NCXAUCR40-100ML**
Bare Bioready Carbonate for Passive Adsorption in Water	40	**NCXAUKR40**
Bare Bioready Carbonate for Passive Adsorption in Aqueous Potassium Carbonate	80	**NCXAUKR80-25ML** **NCXAUKR80-100ML** **NCXAUKR80-500ML** **NCXAUKR80-1000ML**

Gold Nano-urchins

Particle Size (nm)	Absorption	Cat. No.
60	585 nm	**795399-25ML**
50	585 nm	**795380-25ML**
100	680 nm	**797758-25ML**
70	600 nm	**797731-25ML**
80	620 nm	**797723-25ML**
90	630 nm	**797707-25ML**

Surface Functionalized Nanoparticles & Nanostructures

Gold Nanoparticles

Description	Dimension (nm)	Absorption	Cat. No.
PEG 3000 coated amine functionalized	5	λ_{max} 515 nm	**765260-1ML**
	10	λ_{max} 520 nm	**765295-1ML**
	15	λ_{max} 520 nm	**765317-1ML**
	20	λ_{max} 520 nm	**765333-1ML**
	30	λ_{max} 525 nm	**765368-1ML**
	40	λ_{max} 530 nm	**765384-1ML**
	50	λ_{max} 535 nm	**765406-1ML**
PEG 5000 coated amine functionalized	5	λ_{max} 515 nm	**765279-1ML**
	10	λ_{max} 520 nm	**765309-1ML**
	15	λ_{max} 520 nm	**765325-1ML**
	20	λ_{max} 520 nm	**765341-1ML**
	30	λ_{max} 525 nm	**765376-1ML**
PEG 5000 coated amine functionalized	40	-	**765392-1ML**
PEG 5000 coated amine functionalized	50	λ_{max} 535 nm	**765414-1ML**
PEG 5000 coated biotin terminated	5	λ_{max} 513-517 nm	**808628-0.5ML**
PEG 5000 biotin terminated	10	λ_{max} 515-520 nm	**808709-0.5ML**
	15	peak SPR wavelength 520 nm	**808830-0.5ML**
PEG 5000 coated biotin terminated	20	peak SPR wavelength 524 nm	**808849-0.5ML**
PEG 5000 biotin terminated	30	peak SPR wavelength 526 nm	**808857-0.5ML**
PEG 5000 coated biotin terminated	40	peak SPR wavelength 530 nm	**808865-0.5ML**
PEG 5000 biotin terminated	60	λ_{max} 540 nm	**808911-0.5ML**

Description	Dimension (nm)	Absorption	Cat. No.
PEG 5000 coated biotin terminated	80	peak SPR wavelength 553 nm	**808946-0.5ML**
	100	λ_{max} 572 nm	**808962-0.5ML**
PEG 3000 coated carboxylic acid functionalized	5	λ_{max} 515 nm	**765430-1ML**
PEG 3000 carboxylic acid functionalized	10	λ_{max} 520 nm	**765457-1ML**
PEG 3000 coated carboxylic acid functionalized	15	λ_{max} 520 nm	**765473-1ML**
	20	λ_{max} 520 nm	**765503-1ML**
	30	λ_{max} 525 nm	**765538-1ML**
	40	λ_{max} 530 nm	**765554-1ML**
	50	λ_{max} 535 nm	**765570-1ML**
PEG 5000 coated carboxylic acid functionalized	10	λ_{max} 530 nm	**765465-1ML**
	15	λ_{max} 520 nm	**765481-1ML**
	20	λ_{max} 520 nm	**765511-1ML**
PEG 5000 carboxylic acid functionalized	30	λ_{max} 525 nm	**765546-1ML**
PEG 5000 coated carboxylic acid functionalized	40	λ_{max} 530 nm	**765562-1ML**
	50	λ_{max} 535 nm	**765589-1ML**
methyl terminated, PEG 2000 coated	5	-	**765597-1ML**
PEG 2000 coated methyl terminated	15	λ_{max} 520 nm	**765694-1ML**
	20	λ_{max} 520 nm	**765716-1ML**
methyl terminated, PEG 2000 coated	30	-	**765635-1ML**
	50	-	**765678-1ML**
PEG 5000 coated methyl terminated	5	λ_{max} 515 nm	**765600-1ML**
methyl terminated, PEG 5000 coated	10	-	**765627-1ML**
PEG 5000 coated methyl terminated	15	λ_{max} 520 nm	**765708-1ML**
	30	λ_{max} 525 nm	**765732-1ML**
	50	λ_{max} 535 nm	**765686-1ML**

Gold Nanospheres

Description	Dimension (nm)	Cat. No.
Bioready Carboxyl for Covalent Conjugation in Water	40	**NCXAUXR40-5ML** **NCXAUXR40-30ML** **NCXAUXR40-100ML**
	80	**NCXAUXR80-5ML** **NCXAUXR80-30ML** **NCXAUXR80-100ML**
Dried Econix PVP 40 kDa (Polymer)	15	**NCXGEPD15-50MG** **NCXGEPD15-125MG** **NCXGEPD15-500MG**
	50	**NCXGEPD50-50MG** **NCXGEPD50-125MG** **NCXGEPD50-500MG**
	75	**NCXGEPD75-50MG** **NCXGEPD75-125MG** **NCXGEPD75-500MG**
Econix PVP 40 kDa (Polymer)	15	**NCXGEPE15-10ML** **NCXGEPE15-25ML** **NCXGEPE15-100ML**
	50	**NCXGEPE50-10ML** **NCXGEPE50-25ML** **NCXGEPE50-100ML**
	75	**NCXGEPE75-10ML** **NCXGEPE75-25ML** **NCXGEPE75-100ML**
NanoXact Silica (Silanol) Silica-Shelled	20	**NCXAUSH20-1ML** **NCXAUSH20-5ML** **NCXAUSH20-10ML**
	50	**NCXAUSH50-1ML** **NCXAUSH50-5ML** **NCXAUSH50-10ML**
	70	**NCXAUSH70-1ML** **NCXAUSH70-5ML** **NCXAUSH70-10ML**
	100	**NCXAUSH100-1ML** **NCXAUSH100-5ML** **NCXAUSH100-10ML**

Description	Dimension (nm)	Cat. No.
Aminated / Cationic Silica NanoXact Silica-Shelled	20	**NCXAUAH20-1ML** **NCXAUAH20-5ML** **NCXAUAH20-10ML**
	50	**NCXAUAH50-1ML** **NCXAUAH50-5ML** **NCXAUAH50-10ML**
	70	**NCXAUAH70-1ML** **NCXAUAH70-5ML** **NCXAUAH70-10ML**
	100	**NCXAUAH100-1ML** **NCXAUAH100-5ML** **NCXAUAH100-10ML**
Bioready Streptavidin in Aqueous Conjugate Buffer with Streptavidin	40	**NCXAUIR40-200UL** **NCXAUIR40-1ML** **NCXAUIR40-5ML** **NCXAUIR40-10ML**
PEG Carboxyl 0.8 kDa Ultra Uniform	10	**NCXAUXU10-1ML** **NCXAUXU10-5ML** **NCXAUXU10-10ML** **NCXAUXU10-30ML**
	30	**NCXAUXU30-1ML** **NCXAUXU30-5ML** **NCXAUXU30-10ML** **NCXAUXU30-30ML**
	50	**NCXAUXU50-1ML** **NCXAUXU50-5ML** **NCXAUXU50-10ML** **NCXAUXU50-30ML**
	100	**NCXAUXU100-1ML** **NCXAUXU100-5ML** **NCXAUXU100-10ML** **NCXAUXU100-30ML**

Gold Nanorods

Description	Dimension (nm)	Absorption	Cat. No.
amine terminated	10	808 nm	**716871-1ML**
carboxyl terminated	10	808 nm	**716898-1ML**

Gold Nanoparticles for Biomolecular Diagnostics


Alexandra R. Fernandes[1] and Pedro V. Baptista[1*]

[1] UCIBIO, Dept. of Life Sciences, FCT-NOVA, Campus Caparica, 2829-516 Caparica, Portugal
* Email: pmvb@fct.unl.pt

Introduction

Research in nanomedicine has advanced many biomedical tools and applications of nanomaterials, primarily focused on new diagnostic platforms and strategies for therapy. While drug delivery was the first area to be more thoroughly examined and developed over the years, a more profound understanding of nanomaterial properties has allowed for the design of innovative diagnostics strategies. The unique properties of nanomaterials, coupled with the growing capability for tight control over manipulation and assembly, have furthered the concept of combining diagnosis and delivery into one device as an essential asset to allow precise treatment. Thus, nanomedicine may be perceived as a refinement of molecular medicine, integrating innovation in genomics and proteomics for more personalized medicine, allowing the precise characterization of molecular profiles of patients, from early diagnosis to precision therapeutics, improving outcomes while minimizing risks to the patients.[1-2]

These nanometric structures have found a wide range of applications within the biomedical field, with a particular focus on diagnostics, such as detection and identification of metabolites, proteins, and nucleic acids (DNA and RNA). Perhaps the most significant impact has been in molecular diagnostics, where the use of nanomaterials has prompted a change of paradigm in biodetection and analytical methodologies. Within this framework, diagnostic techniques based on nanoparticles offer an unprecedented gain in terms of sensitivity. Since most biomarkers are within a similar size range of these nanoscale structures, providing a 1:1 scale ratio response; this gain in sensitivity also allows to use of less sample, thus decreasing the need for robust apparatus for analytical procedures, which result in increased portability, bringing the conceptual lab to the point-of-need (patient bedside, clinician's lab, etc.).[3]

Synthesis and Functionalization of Gold Nanoparticles

Most platforms designed for protein detection customarily rely on molecular recognition using antigens and antibodies, whereas those designed towards nucleic acid-sensing rely on the complementarity of nucleotide sequences via hybridization protocols. Currently, biodetection of relevant nucleotide sequence biomarkers has progressively integrated nanoparticle-based systems, increasing sensitivity and lowering costs. Among these, noble metal nanoparticles (NPs), particularly gold, due to their optical and physic-chemical properties, have been used for the development of highly sensitive biosensing platforms.[3]

A key feature of AuNPs is their localized surface plasmon resonance (LSPR) that is responsible for their remarkable optical properties. The LSPR may be defined as the collective oscillation of electrons between empty orbitals in response to an incident electromagnetic wave, which generates a polarization in the nanoparticles, inducing the formation of dipolar moments. The LSPR is highly dependent on the size, shape, composition, distance between nanoparticles, and their interaction with the dielectric surrounding. This phenomenon is responsible for attributing different colors to colloidal suspensions of AuNPs, which can vary from different shades of red to blue and purple. Therefore, tight control of the AuNP size is paramount to tune the optical properties towards the desired biodetection wavelength. Also, to take full advantage of these optical properties, different routes for synthesis, means for dispersion in solution, and strategies for surface functionalization may be employed.[3,4]

The most common and straightforward method for synthesis of AuNPs is through the chemical reduction of gold salt, usually tetrachloroauric acid trihydrate ($HAuCl_4 \cdot 3H_2O$), in the presence of reducing agents, such as sodium borohydride, ascorbic acid, or sodium citrate, which bind to the surface of the particles providing stability, reactivity and specific charge properties. Sodium citrate, for example, has been used since 1951 to produce monodisperse nanoparticles with sizes ranging from 1 to 150 nm.[5] Although chemical reduction of metal ions is the most widespread method for synthesizing metal nanoparticles, some of these reducing agents are toxic, expensive, and their residues can be incorporated into the nanostructure, making characterization difficult and limiting *in vivo* applications. Furthermore, the control of process variables, such as pH and temperature, is critical for obtaining a homogeneous particle size dispersion.[6] Due to its simplicity, while offering reasonable control over size dispersion and shape, the citrate reduction method proposed by Turkevich and later optimized by Frens makes it the most widespread method to produce AuNPs for biomedical applications.[3,5,7,8] By simply varying the amount of reducing agent (e.g., sodium citrate) added to the mixture, it is possible to scale up production with reasonable size control (**Figure 1**). For example, when using a lower concentration of sodium citrate, the particle diameter produced is greater, and consequently, the number of agglomerates is greater. In fact, this process yields better results for smaller nanoparticles (10–30 nm in diameter), which are also more stable and, consequently, have less tendency to agglomerate and provide for better and more reproducible results down the line in biodetection. The stability of the colloidal AuNPs solutions depends on their interaction with the surrounding medium, either via electrostatic stabilization (ionic interactions, in which nanoparticles repel each other due to the presence of charged molecules on the surface) or steric stabilization mediated by covalent interactions with suitable moieties that prevent the approach of other AuNPs. Covalent interactions provide some advantages compared to ionic interactions, where modified AuNPs (e.g., bioconjugates) show a considerable increase in stability in diverse media.[6,8]

One way to minimize the tendency for the AuNPs to agglomerate is via the modification of the nanoparticle surface by the use of surfactants, polyelectrolytes, or ligands. Not only this improves colloidal stability, but it also provides for the possibility to derivatize AuNPs with a plethora of biomolecules suitable for biorecognition, such as antibodies and DNA/RNA oligomers. Still, the functionalization process quality is directly affected by factors such as substrate roughness, time of contact with the surface, concentration of the solvent, and temperature of the medium. In addition, the conjugated layers topography faithfully reproduces the surface of the AuNP and, consequently, its surface defects. One of the main types of defects found on gold surfaces is monoatomic vacancy, i.e., the surface presents irregularities, such as the reduction of gold atoms, directly affecting the formation, organization, and efficiency of functionalization.[6,8,9]

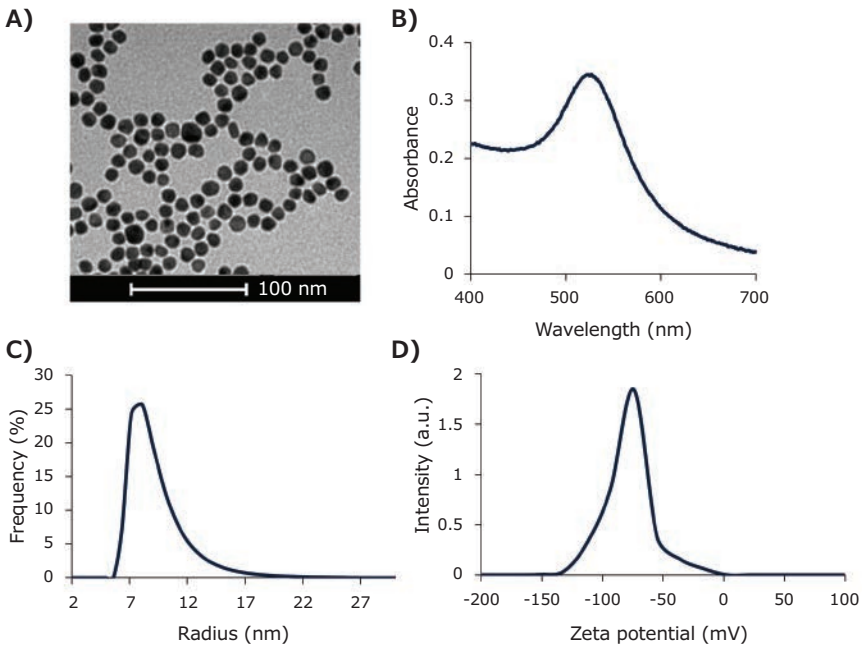

Figure 1. Characterization of AuNPs synthesized by the citrate reduction method. Several standard and straightforward techniques used for characterization of AuNPs, such as **A**) Transmission Electron Microscopy (TEM), showing the spherical shape with good size dispersion; **B**) UV-visible spectroscopy, where the LSPR peak is used for the assessment of size and stability; **C**) Dynamic Light Scattering (DLS), which measures the hydrodynamic radii of AuNPs, thus highlighting the size dispersion; and **D**) zeta potential, which provides information of the superficial charge of the AuNPs, thus an assessment of stability. Altogether, these data are easy to acquire and provide enough information for manufacturing characterization.

Generally, for the surface functionalization of AuNP, the so-called alkanethiols are used for chemical stability and easy formation of self-organizing monolayers. Several stabilizing agents and polymeric compounds may also be used, such as sodium citrate, cetrimonium bromide (CTAB), polyethylene glycol (PEG), silica, among others.[6,8] The choice of stabilizing agent is critical for diagnostics applications; this interface is often used as a linker for the biorecognition element (e.g., DNA, RNA, aptamer, peptides, antibodies) that should not disturb the intrinsic nanoscale property being used for signal transduction upon recognition of target analyte. This stabilization of AuNPs can also be steered through multifunctional polymers with the capability to bind the gold surface and provide for the simultaneous biding to the recognition element (e.g., methyl, amino, carboxyl, carbonyl, hydroxyl, and even sulfhydryl groups). Perhaps the most used linkers are those relying on (at least) one thiol-reactive group, which binds strongly and spontaneously to gold due to the strong interaction between gold atoms and sulfur. In fact, this is the preferred strategy for directly binding DNA, RNA, and aptamer oligomers to the AuNPs' surface, as shown in a diversity of molecular diagnostics concepts.[10,11]

Antibodies are glycoproteins belonging to the class of immunoglobulins commonly associated with the defense of organisms against foreign antigens. Antibodies can bind to various surfaces and have been used as biorecognition molecules for biodetection, particularly associated with AuNPs. Antibodies have a high degree of affinity and specificity, with the ability to detect, recognize and bind to the target antigen.[12] The principle of the association between an epitope of an antigen and its antibody involves the complementarity between them and a reversible bond via electrostatic interactions, hydrogen bonds, hydrophobic and van der Waals interactions. Since direct functionalization of antibodies to the AuNPs' surface is not as straightforward as for DNA/RNA, the use of heterofunctional polymers such as PEG (HS-PEG-NH_2) provides a route to the nanoparticle functionalization, where there is a covalent bond through the –SH group, while the NH_2 group is available to bind the antibody via free COO- groups. Functionalization is typically achieved via prior activation of one of the many COOH groups of the antibody through the use of coupling agents, such as 1-ethyl-(3-dimethylaminopropyl)-carbodiimide (EDC).[10]

AuNPs for Molecular Diagnostics

Several colorimetric approaches based on AuNPs have been proposed for the detection of biomolecules (i.e., nucleic acid and proteins) with high levels of sensitivity and specificity.[3,13] Most of these methods rely on the colorimetric change of an AuNPs solution upon aggregation, a process that may be mediated either by changes to the media dielectric or interaction with the designated target. In the former, binding and adsorption of the target modulated the effect of changes to the medium dielectric on the AuNPs; the latter relies on the capability of targets to mediate interparticle interactions, either by promoting cross-linking of AuNPs or keeping them apart via steric hindrance. The resulting aggregation leads to a shift of the LSPR band, which may be perceived by the naked eye or measured through standard spectrophotometry. This is the case of several hybridization-based protocols, where ssDNA probes are functionalized onto the AuNPs and used to identify DNA/RNA targets in a sequence-dependent manner (**Figure 2**).[10]

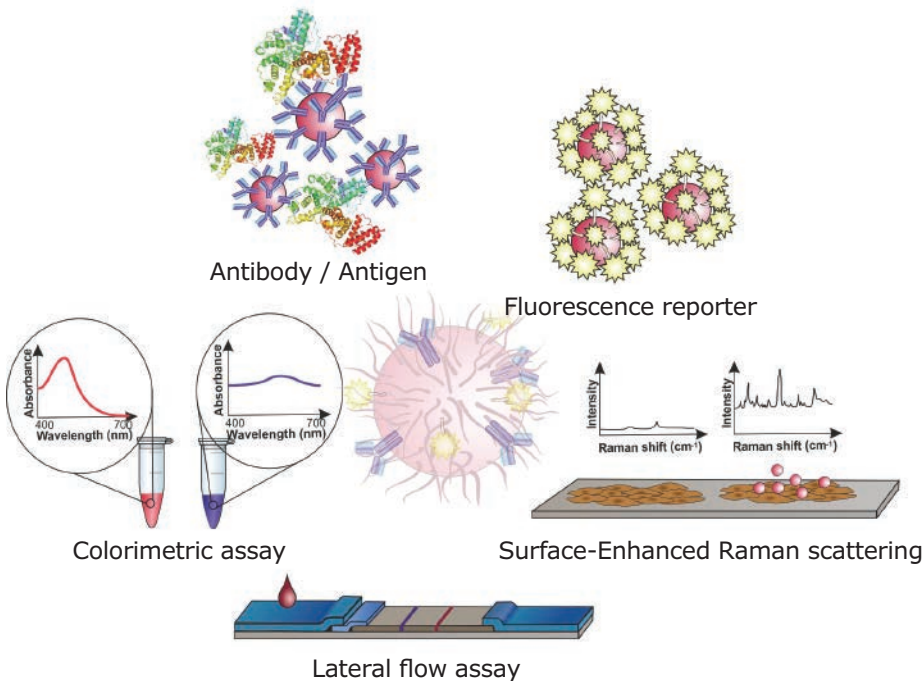

Figure 2. Gold nanoparticles (AuNPs) for molecular diagnostics. AuNPs may be used in a plethora of diagnostics schemes based on antibody-antigen recognition or DNA hybridization, such as colorimetric assays based on inter-particle distance; fluorescence modulation as a function of the distance between the fluorophore and the AuNP surface; Surface Enhanced Raman Spectroscopy (SERS); and the application of AuNPs as tags in lateral flow platforms (LFAs) for point-of-need.

The AuNPs' plasmonic specific and sharp electrical shifts may also be used to detect a biomarker based on light scattering. These approaches rely on the intense scatter of larger and anisotropic AuNPs, whose spectral changes are associated with the binding or association to molecules.[14]

AuNPs are also useful for electrochemical detection, namely, to bind enzymes to electrodes and mediate electrochemical reactions as redox catalysts.[15] In addition, AuNPs are well-known quenchers of fluorescence dyes that are positioned close to their surfaces, a property that has been widely used for molecular detection schemes. In these platforms, binding to the specific target triggers a conformational change of the recognition moiety, which moves the fluorophore further apart from the AuNP or closer to the surface, thus increasing or decreasing the fluorescence emission.[16]

Raman spectroscopy has also profited from the use of AuNPs, particularly the anisotropic and irregular-shaped structures. Surface Enhanced Raman Spectroscopy (SERS) considerably enhances the metal surface association of the intrinsically weak Raman signal intensity of biomarkers. For example, non-spherical AuNPs, where the edges of the nanoparticles act as a hotspot for up to 10^{12} to 10^{14} enhancement of the SERS signal, offer a new dimension to multiplexing detection of biomarkers.[17]

The Case for Lateral Flow Devices

Lateral flow devices (LFA) are portable devices capable of transferring biological fluids, such as blood or serum, through their capillary action, without requiring an external power supply. LFAs are fast and straightforward to handle, low cost, with acceptable specificity without the need for refrigeration. Several diagnostics have primarily incorporated AuNPs as labels/tags for probes, adding sensitivity to the system. The most well-known LFA immunoassay is the pregnancy test; however, any molecule may be a target, and there are already rapid tests for SARS-CoV-2, HIV, HCV, among others.[3,18,19]. The principle mechanism of LFAs is the capillary migration of the biomarkers within the sample towards the region where a first recognition element is conjugated to the AuNPs, typically a capture ssDNA oligomer probe or an antigen/antibody. Then, this complex migrates to the detection region through a hydrophobic nitrocellulose membrane or cellulose acetate and is immobilized by a second recognition/capture element. In the control section of the device, the second capture/recognition element immobilizes the initial complex but not the complex of interest, yielding the result. The striking vibrant red color of the AuNPs makes them ideal tags for these systems, rendering them suitable for evaluation by the naked eye.[3]

Regulations and Standards

The growing number of conceptual devices and platforms for *in vitro* diagnostics using nanomaterials and AuNPs has sparked a need to create standardized methodologies and regulatory protocols for the fabrication and characterization of nanomaterials[20]. However, the worldwide regulatory agencies' capability to regulate these products is limited by the sheer nature and scale of the nanomaterials. One such regulation effort has been undertaken at the Nanotechnology Characterization Laboratory (NCL), a formal scientific interaction of three US Federal agencies: National Cancer Institute (NCI), Food and Drug Administration (FDA), and National Institute of Standards and Technology (NIST), created to support the growing need for characterization and standardization. The proposed guidelines and protocols span over physic-chemical characterization (i.e., size, morphology, shape, surface charge, etc.), *in vitro* characterization (i.e., sterility, drug release, targeting, toxicity, etc.), and *in vivo* characterization (i.e., efficacy, exposure, etc.).

The International Organization for Standardization (ISO) has already implemented some guidelines and certifications, such as ISO/TS 12901: 2012 for the management of risks applied to nanomaterials engineering; ISO/TR 11360: 2010 for classification of nanomaterials, ISO/TS 12025: 2012 for quantification of NOAAs generated by aerosols, and ISO/TS 16195: 2013 with guidelines for tests on materials incorporating nanoscale parts. All the guidelines and certifications must be aligned with the more general directive governing the production and commercialization of *in vitro* diagnostics (IVD) (Directive 98/79/EC of the European Parliament and the Council of 27 October 1998 on *in vitro* diagnostic medical devices). Despite these efforts for standardization, the estimated time to market molecular diagnostics systems incorporating nanoparticles and nanomaterials is still considerably long.

Promises and Challenges

Despite significant advances in the use of AuNPs for molecular diagnostics, much remains to be investigated, including improving the robustness and reproducibility of the proposed systems. Perhaps the biggest challenge is the production scale-up of the most innovative concepts and their translation to use in clinics. Several concerns about the control and characterization of each manufactured batch of nanoparticles and subsequent functionalization need careful evaluation under the existing regulatory guidelines and require suitable methods for the required quality control. For all these innovative systems based on AuNPs to reach the *in vitro* diagnostics market, they must abide by the emergent standards and regulations associated with the existing ISO certificates and guides to impact and change the way we perform diagnostics.

Acknowledgments

The authors wish to thank FCT/MCTES for funding to UCIBIO (UIDB/04378/2020). We also thank Catarina Roma-Rodrigues for graphical support.

References

(1) Paunovska, K.; Loughrey, D.; Sago, C. D.; Langer, R.; Dahlman, J.E. *Adv. Mater.* **2019**, *43*, e1902798. doi: 10.1002/adma.201902798.
(2) Greish, K.; Mathur, A.; Bakhiet, M.; Taurin, S. *Ther. Deliv.* **2018**, *9*, 269–285. doi: 10.4155/tde-2017-0118.
(3) Cordeiro, M.; Ferreira Carlos, F.; Pedrosa, P.; Lopez, A.; Baptista, P. V. *Diagnostics* (Basel) **2016**, *6*, 43. doi: 10.3390/diagnostics6040043.
(4) Herizchi, R.; Abbasi, E.; Milani, M.; Akbarzadeh, A. *Artif. Cells Nanomed. Biotechnol.* **2016**, *44*, 596–602.

(5) Turkevich, J.; Stevenson, P. C.; Hillier, J. Faraday Discussions **1951**, *11*, 55–75. doi: 10.1039/df9511100055.
(6) Carnovale, C.; Bryant, G.; Shukla, R.; Bansal, V. *Prog. Mater. Sci.* **2016**, *83*, 152–190. doi:10.1016/j.pmatsci.2016.04.003.
(7) Frens, G. *Nat. Phys. Sci.* **1973**, *241*, 20–22. doi:10.1038/physci241020a0.
(8) Hu, X.; Zhang, Y.; Ding, T.; Liu, J.; Zhao, H. *Front Bioeng Biotechnol.* **2020**, *8*, 990. Doi:10.3389/fbioe.2020.00990.
(9) Love, J. C.; Estroff, L. A.; Kriebel, J. K.; Nuzzo, R. G.; Whitesides, G.M. *Chem Rev.* **2005**, *105*, 1103–1169. doi: 10.1021/cr0300789.
(10) Conde, J.; Dias, J .T.; Grazú, V.; Moros, M.; Baptista, P. V.; de la Fuente, J. M. *Front. Chem.* **2014**, *2*, 48. doi:10.3389/fchem.2014.00048.
(11) Graczyk, A.; Pawlowska, R.; Jedrzejczyk, D. Chworos, A. *Molecules* **2020**, *25*, 204. doi:10.3390/molecules25010204.
(12) Morales, M. A.; Halpern, J. M. *Bioconjug. Chem.* **2018**, *29*, 3231–3239. doi:10.1021/acs.bioconjchem.8b00592
(13) Chang, C. C.; Chen, C. P.; Wu, T. H.; Yang, C. H.; Lin, C. W.; Chen, C. Y. *Nanomaterials* (Basel) **2019**, *9*, 861. doi: 10.3390/nano9060861.
(14) Yang, C. T.; Xu, Y.; Pourhassan-Moghaddam, M., et al. *Sensors* (Basel) **2019**, *19*, 323. doi:10.3390/s19020323.
(15) Rasheed, P.A.; Sandhyarani, N. *Microchim Acta* **2017**, *184*, 981–1000. doi:10.1007/s00604-017-2143-1.
(16) Bouché, M.; Hsu, J. C.; Dong, Y. C.; Kim, J.; Taking, K.; Cormode, D. P. *Bioconjug Chem.* **2020**, *31*, 303–314. doi: 10.1021/acs.bioconjchem.9b00669.
(17) Kasera, S.; Herrmann, L.; Barrio, J.; et al. *Sci. Rep.* **2014**, *4*, 6785. Doi:10.1038/srep06785.
(18) Huang, C.; Wen, T.; Shi, F. J; Zeng, X. Y.; Jiao, Y. J. *ACS Omega* **2020**, *5*, 12550–12556. doi:10.1021/acsomega.0c01554.
(19) Kim, H.; Chung, D.- R.; Kang; M. *Analyst* **2019**, *144*, 2460–2466. doi:10.1039/C8AN02295J.
(20) Baer, D. R. *Surf. Interface Anal.* **2012**, *44*, 1305–1308. doi:10.1002/sia.4938.

Surface Functionalized Nanoparticle & Nanostructure Kits

Gold Nanoparticles

Functional Group	Particle Size (nm)	Absorption	Cat. No.
NHS ester	5	515-520 nm	**900470-1EA**
	10	515-520 nm	**900473-1EA**
	15	520 nm	**900474-1EA**
	20	524 nm	**900475-1EA**
	30	526 nm	**900476-1EA**
	40	530 nm	**900477-1EA**
	50	535 nm	**900478-1EA**
	60	540 nm	**900479-1EA**
	70	548 nm	**900480-1EA**
	80	553 nm	**900481-1EA**
	90	564 nm	**900482-1EA**
	100	572 nm	**900483-1EA**
maleimide	5	515-520 nm	**900458-1EA**
	10	515-520 nm	**900459-1EA**
	15	520 nm	**900460-1EA**
	20	524 nm	**900461-1EA**
	30	526 nm	**900462-1EA**
	40	530 nm	**900463-1EA**
	50	535 nm	**900464-1EA**
	60	540 nm	**900465-1EA**
	70	548 nm	**900466-1EA**
	80	553 nm	**900467-1EA**
	90	564 nm	**900468-1EA**
	100	572 nm	**900469-1EA**

Gold Nanoshells

Name	Description	Particle Size (nm)	Cat. No.
Gold Nanoshells	Bioready Dried NHS Small Reaction Kit (with 10 Spin Filters) for Conjugation	150	**NCXGSNR15010S-1KT**
	Bioready Dried Large Reaction Kit (with 1 Spin Filter) NHS for Conjugation	150	**NCXGSNR1501L-1KT**
	Bioready Dried NHS Small Reaction Kit (with 3 Spin Filters) for Conjugation	150	**NCXGSNR1503S-1KT**

Gold Nanospheres

Name	Description	Particle Size (nm)	Cat. No.
Gold Nanospheres	Bioready Dried NHS Small Reaction Kit (with 10 Spin Filters) for Conjugation	40	**NCXAUNR4010S-1KT**
	Bioready Dried NHS Small Reaction Kit (with 3 Spin Filters) for Conjugation	40	**NCXAUNR403S-1KT**
	Bioready Dried Large Reaction Kit (with 1 Spin Filter) NHS for Conjugation	40	**NCXAUNR401L-1KT**

Gold Nano-urchins

Functional Group	Particle Size (nm)	Absorption (nm)	Cat. No.
maleimide	50	585	**900484-1EA**
	60	585	**900485-1EA**
	70	600	**900486-1EA**
	80	620	**900487-1EA**
	90	630	**900488-1EA**
	100	680	**900489-1EA**
NHS ester	50	585	**900490-1EA**
	60	585	**900491-1EA**
	70	600	**900492-1EA**
	80	620	**900493-1EA**
	90	630	**900494-1EA**
	100	680	**900495-1EA**

Recent Advances on Nanoparticle-Based Imaging Contrast Agents for *In Vivo* Stem Cell Tracking






Chang Xu, Qishuai Feng, Peng Ning, Zhenguang Li, Yao Qin, Yu Cheng*

Translational Medical Center for Stem Cell Therapy & Institute for Regenerative Medicine, Shanghai East Hospital, Tongji University School of Medicine, 1800 Yuntai Road, Shanghai, 200123, China.
* E-mail: yucheng@tongji.edu.cn

Introduction

With their great potential in tissue engineering, regenerative medicine, and homing effect, stem cell therapies are promising strategies for treating many incurable diseases, such as Parkinson's disease, liver failure, ischemic heart disease, and cancer. The cell distribution state, migration behaviors, and functionality after engraftment cannot be well elucidated due to a lack of effective *in vivo* tracing methods, thus impeding the clinical transformation of stem cell therapies. Developing more advanced imaging strategies to label and track transplanted stem cells without affecting their normal physiological functions is necessary to reveal their therapeutic mechanisms and evaluate their safety before clinical trials. The ideal imaging techniques for stem cells should be non-toxic and high-resolution, have an extended life, and dynamically provide the cell fate information. A variety of bioimaging strategies have been developed over the past few years. One promising strategy uses well-designed nanoparticles as contrast agents to track stem cells, due to their distinguished physiochemical properties as well as their designability and versatility. Despite this, the existing imaging methods cannot satisfy all the *in vivo* stem cell tracking requirements. Herein, we provide a brief review of the four most commonly used nanoparticle-based imaging modalities for stem cell tracking: magnetic resonance imaging (MRI), fluorescence imaging, ultrasound imaging (USI), and photoacoustic imaging (PAI) (**Figure 1**). Special attention is paid to the design of contrast nanoagents, the corresponding imaging mechanism, and the issues these nanoagents have resolved. This serves to shed light on the future design and fabrication of more advanced contrast agents, approaching an ideal one for tracking transplanted stem cells *in vivo*.

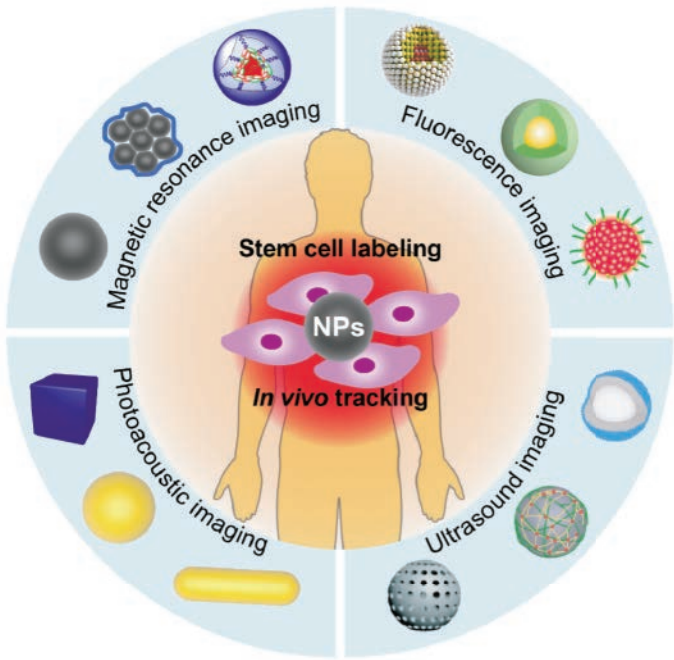

Figure 1. Various contract nanoagents designed for magnetic resonance imaging, fluorescence imaging, ultrasound imaging, and photoacoustic imaging modalities in stem cell tracking *in vivo*.

Magnetic Resonance Imaging (MRI)

Magnetic resonance imaging (MRI) is the preferred method for *in vivo* stem cell imaging due to its unique features, including no penetration depth limitation, excellent spatial (40 to 100 μm) and temporal (minutes to hours) resolution, and safe operation.[1] There are two categories of MRI: T1/T1*or T2/T2*-weighted MRI, based on the relaxation time of the longitudinal (T1) and transverse (T2) components of the magnetization vector towards equilibrium under the applied magnetic field. MRI contrast agents, including gadolinium (III) chelates and superparamagnetic iron oxide nanoparticles (SIONPs), are introduced to achieve a higher resolution and enhance the signal intensity by altering the relaxation times of surrounding water protons.[2] Gadolinium(III) chelates are effective T1 contrast agents because they shorten the longitudinal relaxation rate (T1) and increase positive contrast on T1-weighted MRI sequences. As a T2 contrast agent, SIONPs have widely been applied in the field of MRI-based cell tracking to provide negative contrast by shortening the T2/T2* relaxation time. In the following section, nanoparticle-based contrast agents with clinical or commercial proof are reviewed for use in applications in stem cell tracking.

The fundamental requirements for nanoparticle-based stem cell labeling agents include colloidal stability, non-toxicity, high magnetism, and labeling efficiency. Colloidal stability in aqueous solution was typically obtained using hydrophilic polymer coatings, such as chitosan, dextran, PEG, etc. Margarita Gutova et al. reported a preclinical study where neural stem cells (NSCs) labeled with dextran coated ferumoxytol (FDA approval SIONPs) were transplanted into the patients with brain tumors[3] NSC distribution was steadily and continuously tracked at multiple points for 12 weeks, followed by surveillance serial MRI.[3] High labeling efficiency can also be obtained by modifying the particle surface to have a positive charge or specific ligands. For example, compared to ferumoxytol itself, self-assembling ferumoxytol nano-complexes modified with heparin and protamine sulfate, which reversed the negative charge of the original particle, showed higher labeling efficiency, and a threefold increase in T2 relaxivity. This modification strategy displayed *in vivo* MRI detection of at least 1,000 HPF-labeled cells implanted in rat brains.[4] In addition, clinically approved Gd-DTPA wrapped with cationic liposomes could assure a highly efficient uptake of Gd and excellent intracellular retention in mesenchymal stem cells. Gd-DTPA-liposomes complex contrast agent made 500,000 labeled stem cells clearly visible for at least 2 weeks on a 3.0 T clinical scanner, thus overcoming the relatively low MRI sensitivity of Gd-DTPA.[5]

Monitoring migration and survival of stem cells are critical for therapeutic efficacy and safety assessments. For tracking stem cell migration, Lili Jiang et al. found that T2*-weighted MRI could monitor the migration of implanted pluripotent stem cells labeled with SIONPs (Sigma-Aldrich, Darmstadt, Germany) from the injection site to the injured brain areas over 4 weeks.[6] In evaluating cell survival, Ashok J. Theruvath et al. reported ferumoxytol-labeled apoptotic matrix-associated stem cell implants (MASIs) showed a significant loss of iron signals and longer T2 relaxation time viable 2 weeks after implantation in a cartilage repair process.[7] When combined with a histopathologic examination, a ferumoxytol-based contrast agent can act as an indicator of the living or dead stem cells.

According to specific tissues, organs, and diseases, the stem cell tracking window ranges from several days to months. The strategy for *in vivo* tracking stem cells requires assessing the distribution, migration, and differentiation of the cells, as well as the efficacy and safety of cell implantation. Despite the rapid development in nanoparticle-based MRI for stem cell tracking, some challenges remain, such as imaging the differentiation and function of stem cells, combining MRI contrast agents with reporter genes, and coupling MRI with other noninvasive imaging tools.

Fluorescence Imaging

Fluorescence imaging is a classical optical imaging technology. Although being low cost and highly sensitive, it has poor tissue penetration (<1 cm) when compared to MRI technology. A solution to this issue is to tune the fluorophore or fluorescent protein to be excited in the near-infrared (NIR) range for deeper infiltration. However, the severe photo-bleaching and light scattering limits the tracking time and efficiency.[8] The development of fluorescent nanoparticles (NPs) has improved the ability of fluorescent imaging in long-term tracing stem cells *in vivo*.

Quantum dots (QDs) are a series of classical inorganic semiconductor NPs for cell labeling.[9] QDs optical abilities are based on the transition behaviors of excited electrons between different energy levels, which can be modulated via manipulating the material components or compositions to realize the NIR emission. For example, CdSe/ZnS core/shell structures were designed to label and trace adipose tissue-derived stem cells (ASCs) in C57BL/6 mice models under NIR emission.[10] By changing the bandgap, the material design can significantly improve the optical properties of the QDs.[11] Wang et al. combined a NIR-II fluorescence QDs of Ag_2S with classical bioluminescence red firefly luciferase (RFLuc) to label human mesenchymal stem cells (hMSCs). They studied the dynamic tracking of the survival and osteogenic differentiation of the transplanted hMSCs in a calvarial defect mouse model in a wide window of 400–1700 nm.[12] Up-conversion nanoparticles (UCNPs), which depend on the shining mechanism of the anti-Stocks process through absorbing several NIR photons to generate one single short-wavelength photon, have also been used to label and track mouse MSCs.[13,14] Nevertheless, heavy metal ions in QDs and rare earth metal ions doped in UCNPs are potential safety hazards for clinical stem cell tracing. Aggregation-induced emission (AIE) fluorophores provide the potential to track stem cells with satisfying security and excellent photostability when compared with inorganic NPs.[15–18] AIE fluorophores are non-emissive in the dispersive state but emit strong fluorescence under the aggregative state due to the restriction

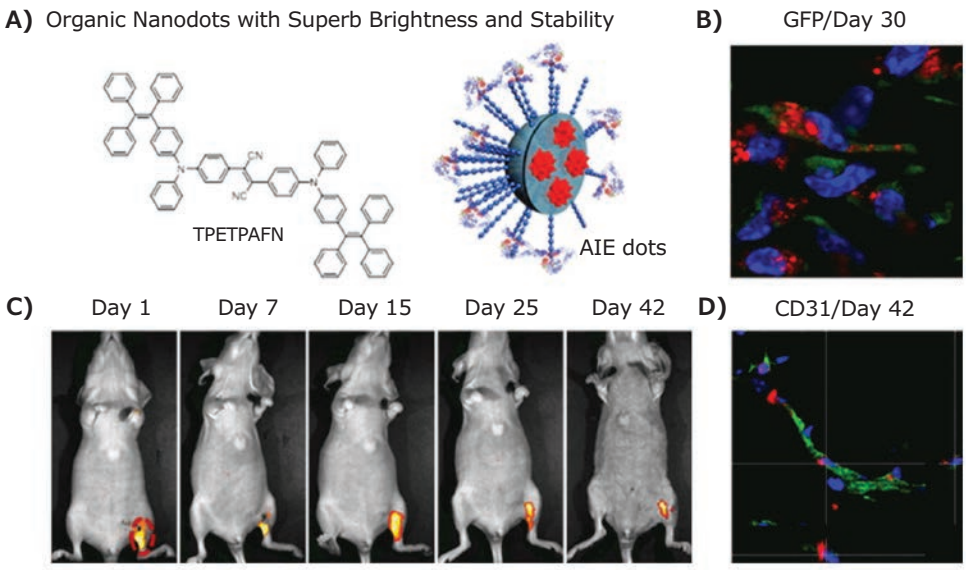

Figure 2. A) Structure of single AIE molecular (TPETPAFN) and schematic of the aggregated AIE dots. B) Representative confocal laser scanning microscopy (CLSM) images of ischemic hind limb slices from mice, administrated with AIE dot-labeled ADSC-containing matrigels for 30 days. C) Representative *in vivo* fluorescence images of the ischemic hind limb-bearing mouse was intramuscularly treated with AIE dot-labeled ADSC-containing matrigel. D) Representative CD31-staining 3D sectional CLSM image of ischemic hind limb slices from mice injected with AIE dot-ADSC-M for 42 days. Adapted with permission from reference 18, copyright 2014 American Chemical Society.

of intramolecular rotation, which is opposite to aggregation caused quenching (ACQ). This unique feature makes AIE NPs or Dots present enduring and stable fluorescent signals. For instance, AIE Dots based on the tetraphenyl ethylene derivative have proven to be capable of tracing the fate of adipose-derived stem cells (ADSCs) in a long-term manner compared with green fluorescent proteins (FPs) or other bioluminescence molecules (**Figure 2**).[18] Additionally, the AIE monomer can easily be designed and adjusted for NIR or even NIR-II emission. The development of AIE Dots is a promising alternative for tracking stem cells with long-term and high stability *in vivo*.

Ultrasound Imaging

With the advantages of excellent temporal and spatial resolution and significant tissue penetration depth, ultrasound imaging is a powerful tool for long-term and noninvasive cell tracking in stem cell-based therapies.[19] However, it is limited by the poor contrast between engrafted cells and adjacent soft tissues. Ultrasound contrast agents (UCAs), a class of echogenic materials, are used in clinics to significantly improve the contrast and enhance the echoing signals in detection.[20] Conventional UCAs are micro-sized, gas-filled microbubbles composed of a bioinert heavy gas surrounded by stabilizing shells, such as lipids, proteins, and biocompatible polymers.[21] The potential utility of these microbubbles in stem cell tracking has been constrained by their large microscale size, poor structural stability, and short half-life.

Recently, research has focused on the miniaturization of UCAs, and nanoscale UCAs, such as nanobubbles, silica nanoparticles, and nanotubes, have been developed for ultrasound imaging.[22] For nanobubbles, stabilizing the shell structure is a prerequisite. Leon et al. reported a type of ultrastable nanobubble by adapting a bilayer shell architecture with contrasting elastic properties similar to bacterial cell envelopes.[23] The ultrastable nanobubbles have minimal signal attenuation when treated with ultrasound waves continuously *in vitro* and have a longer half-life *in vivo*. However, nanobubbles may not have sufficient echogenicity because they are too small to scatter ultrasonic waves efficiently. A "small to large" transformation strategy has been proposed to solve this problem, in which the nanoscale UCAs can transform into microbubbles under ultrasonic irradiation, thereby enhancing the echoing signals.[24] Gas-generating nanoparticles are typical examples of this aspect.[25,26] Min et al. presented a carbonate copolymer nanoparticle with a unique chemical gas-generating mechanism, where the nanoparticles are hydrolyzed to produce microscale CO_2 bubbles that efficiently absorb ultrasonic energy.[27] For silica nanoparticles and other glass-based nanomaterials, the ultrasound signal is significantly enhanced by the inhomogeneity in the tissue due to the rigid features of these nanoparticles, which display high impedance mismatch at the interface of tissue.[28] Chen et al. described a novel exosome-like silica (ELS) nanoparticle with high ultrasound impedance mismatches for stem cell labeling and tracking.[29] They found that the unique discoid shape of the nanoparticles, along with their positive charge, facilitated cell uptake and inherently increased echogenicity. In addition, silica nanoparticles with other complex structures, including hollow and mesoporous structures, have shown significant ultrasound contrast.[30] These silica-based nanoparticles are promising as UCAs for real-time stem cell tracking via ultrasound imaging owing to their relatively high structural stability, low toxicity, and adjustable structure and size.

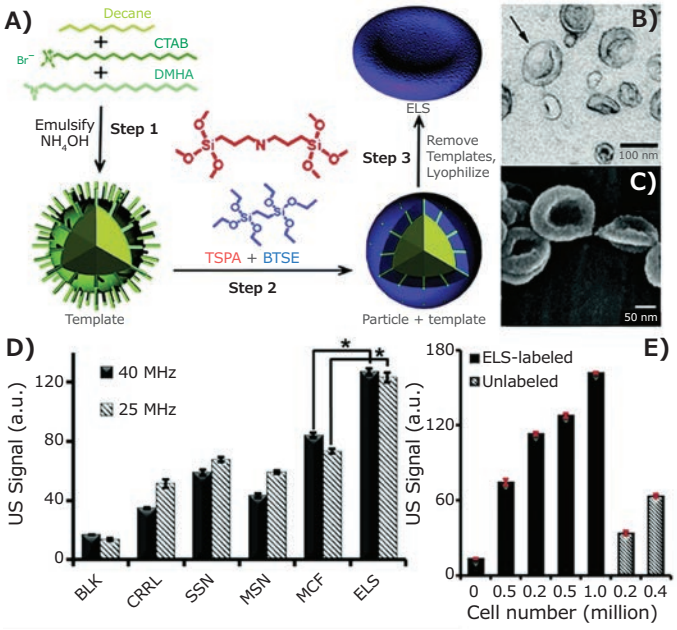

Figure 3. A) Schematic of the novel ELS nanoparticles prepared via an emulsion template method. B) TEM image of typical exosomes. C) SEM image of ELS nanoparticles that are similar to exosomes. D) The echogenicity of human mesenchymal stem cells (hMSCs) increased by ELS. E) Quantification of *in vivo* echogenicity of unlabeled and ELS-labeled hMSCs. Reproduced with permission from reference 29, copyright 2017 Royal Society of Chemistry.

Photoacoustic Imaging

Biosafety and accurate imaging are required for long-term cell tracking *in vivo*. Photoacoustic imaging (PAI) is a promising biomedical imaging modality based on the photoacoustic effect principle.[31] In detail, the introduction of a pulsed laser generates heat, and the intermittent heat causes expansion, detected by PAI as a mechanical wave. This imaging modality combines the high contrast of optical imaging with deep penetration of ultrasonic imaging, providing real-time and high-resolution information *in vivo*.

PAI contrast nanoagents are widely used *in vivo* to image stem cells due to their excellent photothermal conversion ability and the biocompatibility of nanoparticles. The development of various PAI contrast nanoagents allows the absorption of light from visible light to the near-infrared II region, aiming to reduce the light absorbance and scattering from tissues. Tracking methods merely providing physical information, such as locations, of labeled stem cells do not meet stem cell engraftment study requirements. New platforms to indicate the cell function and viability in real-time are needed for clinical applications. By paying particular attention to the design of contrast nanoagents, recent studies of PAI-based stem cell tracking were summarized in the following aspects: component, shape, size and surface modification, elucidating the critical factors needed for future consideration in PAI contrast agent design (**Table 1**).

Among the reported PAI contrast agents, gold nanoparticles have specific advantages owing to their excellent photothermal conversion efficiency, stable imaging ability, and biosafety. The inert characteristic of gold nanoparticles has a minimal side-effect on cell function.[32] Suggs group used gold nanospheres *in vivo* with different sizes (20 nm, 40 nm, and 60 nm) to label and track mesenchymal stem cells (MSCs).[33] This research illustrated the possibility of loading gold nanoparticles into MSCs for imaging and demonstrated a maintained cell function after loading with nanoparticles. It showed that gold nanoparticles retained in stem cells were detectable within 14 days, indicating the long-term and noninvasive cell tracking by PAI was possible. The anisotropic gold nanoparticles have better photothermal conversion efficiency. Jokerst et al. showed that silica coating could increase the uptake rate of gold nanorods into stem cells up to 5 folds, and the minimum detection limit was down to 100,000 labeled cells *in vivo*.[34]

The transplanted microenvironment *in vivo* is complicated. Ricles et al. used a dual gold nanoparticle system (composed of gold nanorods and gold nanospheres) to track transplanted stem cells and image infiltrated macrophages.[35] These studies showed a new method to distinguish delivered stem cells from infiltrated immune cells, which could partially reveal the mechanism of injury healing. Furthermore, PAI was combined with other imaging modalities to enhance the tracking accuracy. Nam et al. combined PAI with ultrasound imaging to monitor MSCs labeled with citrate-stabilized gold nanospheres.[36] The combined strategy could provide both morphological information via ultrasound imaging and functional information via photoacoustic imaging to give the spatial information of labeled MSCs. Qiao et al. used magnetic resonance and PAI to track iron oxide (IO)@Au core-shell structure labeled MSCs for brain tumor imaging. This system showed potential for planning cell routes and imaging the stem-cell migration towards brain tumors in real-time.[37]

Moreover, nanoparticles with NIR absorption were also developed for stem cell tracking via PAI owing to the better penetration depth of NIR light. Kim et al. used Prussian blue nanoparticles with a strong light absorption at 740 nm for stem cell tracking.[38] *In vivo* cell detection limits can reach 200 cells/μL, and monitoring can last 14 days after injection due to the excellent bio-stability of the nanoagents and their NIR-I detectability. Yin et al. designed a NIR-II organic semiconductor polymer for stem cell tracking by PAI.[39] A 40.6- and 21.7-fold enhancement in subcutaneous and brain imaging were reported, respectively, mainly because of the deep penetration of NIR-II light. To monitor the activities of stem cells after transplantation, Dhada et al. designed a ROS sensitive dye (R775c) coated gold nanorods. In their strategy, the properties that stem cells release ROS to degrade dying cells *in vivo* was utilized to measure the stem cell viability. Therefore, they could simultaneously image the cell viability and position *in vivo* using PAI.[40]

Table 1. The design of nanoparticle-based contrast agents for PAI.

Year	Shape	Surface modification	Charge	Size	Concentration	Tracking period
2011 [33]	Gold nanosphere	poly-L-lysine	+ 30 mV	20, 40, 60 nm	10^{12} nanoparticles/mL	14 days
2012 [34]	Gold nanorod	silica	NA	83× 64 nm	4×10^{13} nanoparticles/mL	4 days
2014 [35]	Dual gold nanoparticle system (rods and spheres)	mPEG–SH for spheres; poly-L-lysine for silica rods	-8.41 mV of spheres, +26 mV of rods	50 nm; 56× 16 nm	Both 10^{12} nanoparticles/mL	7 days
2011 [36]	Gold nanosphere	citrate	NA	20 nm	1.13×10^{11} nanoparticles/mL	*in vitro* study
2018 [37]	IO@Au core-shell structure	mPEG–NH2	NA	82 nm	4 μg/mL	3 days
2017 [38]	prussian blue nanoparticles	Poly(L-lysine)	+33.9 mV	133.8 nm	50 μg/mL	14 days
2018 [39]	organic semiconducting polymer	Poly(L-lysine)	+42 mV	99.9 nm	50 μg/mL	14 days
2019 [40]	Silica coated R775c@gold nanorod	poly-D-lysine	+8 mV	450 nm	20 μg/mL	10 days

Table 2. Comparison of different imaging modalities.

Imaging modality	Magnetic Resonance Imaging	Fluorescence Imaging	Ultrasound Imaging	Photoacoustic Imaging
Advantages	Deep penetration; High spatial resolution; Safety	High sensitivity/resolution; Highly developed device	Safe, deep penetration; Real-time dynamic imaging	High resolution; 3-dimensional imaging
Disadvantages	Signal decays as the material degrades; Signal intensity does not linearly proportional to its concentration	Light bleaching; Superficial imaging; Pedigree tracer requires transfection and has limited optical penetration	Short life and large size of contrast agents	The blood signals interference; laser penetrable imaging

Overall, the main advantages of nanoagents over organic molecules used for PAI imaging are photostability, water solubility, and biocompatibility. Since the limitations of PAI depends on the penetration and photothermal conversion efficiency of contrast nanoagents, developing nanomaterials with better NIR-II responsive properties and biocompatibilities would be a future direction for PAI imaging.

Conclusion and Outlook

The advancement of stem cell-based therapies is highly dependent on the development of stem cell tracking techniques. Current imaging technologies have merits and drawbacks (Table 2). Therefore, the selection of imaging modalities depends on the requirements of specific tissues and imaging depth. A variety of nanoparticles, such as iron oxide nanoparticles, quantum dots, aggregative introduced emission nanoparticles, silica nanoparticles, and gold nanoparticles, have been used for tracing stem cells owing to their unique physical-chemical properties, which could enhance the imaging signals under irradiation. Through elaborately designing their structures and compositions, nanoparticles can significantly improve the performance of existing imaging modalities in terms of imaging resolution, stability, and lifetime.

It should be noted that tracking stem cells *in vivo* remains a significant challenge in the biomedical field. Firstly, the amplitude of the image signal is usually linearly proportional to contrast nanoagent concentration, while the contrast agents in cells are diluted with cell division. Therefore, a new generation of contrast agents which could anti-dilute or stimulate the cell to self-synthesize the contrast nanoagents is highly desirable. Secondly, besides cell division, researches revealed that the nanoparticle amount inside cells reach a balance via endocytosis and exocytosis process, which may cause false positive detection *in vivo*. Further, few contrast agents can image the cell's living state and normal function ability, dramatically restraining the mechanism study of stem cell therapy. Thus, more efforts need to consider this aspect by elaborately designing multifunctional contrast agents. Lastly, further development of both "hardware" imaging devices and "software" nanoparticles of imaging contrast agents are urgently needed to realize precise, long-term, dynamic tracking of transplanted stem cells.

References

(1) Barrow, M.; Taylor, A.; Murray, P.; Rosseinsky, M. J.; Adams, D. *J. Chem. Soc. Rev.* **2015**, *44*, 6733–6748.
(2) Zhang, B.; Yan, W.; Zhu, Y.; Yang, W.; Le, W.; Chen, B.; Zhu, R.; Cheng, L. *Adv. Mater* **2018**, *30*, e1705694.
(3) Gutova, M.; Frank, J. A.; D'Apuzzo, M.; Khankaldyyan, V.; Gilchrist, M. M.; Annala, A. J.; Metz, M. Z.; Abramyants, Y.; Herrmann, K. A.; Ghoda, L. Y.; Najbauer, J.; Brown, C. E.; Blanchard, M. S.; Lesniak, M. S.; Kim, S. U.; Barish, M. E.; Aboody, K. S.; Moats, R. A. *Stem Cells Transl. Med.* **2013**, *2*, 766–775.
(4) Thu, M. S.; Bryant, L. H.; Coppola, T.; Jordan, E. K.; Budde, M. D.; Lewis, B. K.; Chaudhry, A.; Ren, J.; Varma, N. R.; Arbab, A. S.; Frank, J. A. *Nat. Med.* **2012**, *18*, 463–467.
(5) Guenoun, J.; Koning, G. A.; Doeswijk, G.; Bosman, L.; Wielopolski, P. A.; Krestin, G. P.; Bernsen, M. R. *Cell Transplant* **2012**, *21*, 191–205.
(6) Jiang, L.; Li, R.; Tang, H.; Zhong, J.; Sun, H.; Tang, W.; Wang, H.; Zhu, J. *Cell Transplant* **2019**, *28*, 747–755.
(7) Theruvath, A. J.; Nejadnik, H.; Lenkov, O.; Yerneni, K.; Li, K.; Kuntz, L.; Wolterman, C.; Tuebel, J.; Burgkart, R.; Liang, T.; Felt, S.; Daldrup-Link, H. E. *Radiology* **2019**, *292*, 129–137.
(8) Kircher, M. F.; Gambhir, S. S.; Grimm, J. *Nat. Rev. Clin. Oncol.* **2011**, *8*, 677–688.
(9) Yu, Y.; Feng, C.; Hong, Y. N.; Liu, J. Z.; Chen, S. J.; Ng, K. M.; Luo, K. Q.; Tang, B. Z. *Adv. Mater.* **2011**, *23*, 3298–3302.
(10) Yukawa, H.; Kagami, Y.; Watanabe, M.; Oishi, K.; Miyanoto, Y.; Okamoto, Y.; Tokeshi, M.; Kaji, N.; Noguchi, H.; Ono, K.; Sawada, M.; Baba, Y.; Hamajima, N.; Hayashi, S. *Biomaterials* **2010**, *31*, 4094–4103.
(11) Yang, Y. M.; Chen, J.; Shang, X. L.; Feng, Z. J.; Chen, C.; Lu, J. Y.; Cai, J. Y.; Chen, Y. Z.; Zhang, J.; Hao, Y. F.; Yang, X.; Li, Y. X.; Chen, S. Y. *Adv. Sci.* **2019**, *6*, 1901018
(12) Huang, D. H.; Lin, S. Y.; Wang, Q. W.; Zhang, Y. J.; Li, C. Y.; Ji, R.; Wang, M.; Chen, G. C.; Wang, Q. B. *Adv. Funct. Mater.* **2019**, *29*, 1806546.
(13) Wang, C.; Cheng, L.; Xu, H.; Liu, Z. *Biomaterials* **2012**, *33*, 4872–4881.
(14) Wilhelm, S. *ACS Nano* **2017**, *11*, 10644–10653.
(15) Li, K.; Zhu, Z. S.; Cai, P. Q.; Liu, R. R.; Tomczak, N.; Ding, D.; Liu, J.; Qin, W.; Zhao, Z. J.; Hu, Y.; Chen, X. D.; Tang, B. Z.; Liu, B. *Chem. Mater.* **2013**, *25*, 4181–4187.

(16) Li, K.; Yamamoto, M.; Chan, S. J.; Chiam, M. Y.; Qin, W.; Wong, P. T. H.; Yim, E. K. F.; Tang, B. Z.; Liu, B. *Chem. Commun.* **2014**, *50*, 15136–15139.
(17) Gao, M.; Chen, J. J.; Lin, G. W.; Li, S. W.; Wang, L.; Qin, A. J.; Zhao, Z. J.; Ren, L.; Wang, Y. J.; Tang, B. Z. *ACS Appl. Mater. Interfaces* **2016**, *8*, 17878–17884.
(18) Ding, D.; Mao, D.; Li, K.; Wang, X. M.; Qin, W.; Liu, R. R.; Chiam, D. S. Z.; Tomczak, N.; Yang, Z. M.; Tang, B. Z.; Kong, D. L.; Liu, B. *ACS Nano* **2014**, *8*, 12620–12631.
(19) Abou-Elkacem, L.; Bachawal, S. V.; Willmann, J. K. *Eur. J. Radiol.* **2015**, *84*, 1685.
(20) Son, S.; Min, H. S.; You, D. G.; Kim, B. S.; Kwon, I. C. *Nano Today* **2014**, *9*, 525–540.
(21) Li, Y.; Chen, Y.; Du, M.; Chen Zhi-Y. *ACS Biomater. Sci. Eng.* **2018**, *4*, 2716–2728.
(22) Smith, B. R.; Gambhir, S. S. *Chem. Rev.* **2017**, *117*, 901–986.
(23) Leon, A.; Perera, R.; Hernandez, C.; Cooley, M.; Jung, O.; Jeganathan, S.; Abenojar, E.; Fishbein, G.; Sojahrood, A. J.; Emerson, C. C.; Stewart, P. L.; Kolios, M. C.; Exner, A. A. *Nanoscale* **2019**, *11*, 15647–15658.
(24) Liu, J.; Shang, T.; Wang, F.; Cao, Y.; Hao, L.; Ren, J.; Ran, H.; Wang, Z.; Li, P.; Du, Z. *Int. J. Nanomed.* **2017**, *12*, 911–923.
(25) Sun, In-C.; Emelianov, S.; *Nanoscale* **2019**, *11*, 16235–16240.
(26) Gao, S.; Wang, G.; Qin, Z.; Wang, X.; Zhao, G.; Ma, Q.; Zhu, L. *Biomaterials* **2017**, *112*, 324–335.
(27) Min, H. S.; Son, S.; You, D. G.; Lee, T. W.; Lee J.; Lee, S.; Yhee, J. Y.; Lee, J.; Han, M. H.; Park, J. H.; Kim, S. H.; Choi, K.; Park, K.; Kim, K.; Kwon, I. C. *Biomaterials* **2016**, *108*, 57–70.
(28) Ma, M.; Shu, Y.; Tang, Y.; Chen, H. *Nano Today* **2020**, *34*, 100897.
(29) Chen, F.; Ma, M.; Wang, J.; Wang, F.; Chern, S. X.; Zhao, E. R.; Jhunjhunwala, A.; Darmadi, S.; Chen, H.; Jokerst, J. V. *Nanoscale* **2017**, *9* (1), 402–411.
(30) Qi, S.; Zhang, P.; Ma, M.; Yao, M.; Wu, J.; Mäkilä, E., Salonen, J.; Ruskoaho, H.; Xu, Y.; Santos, H. A.; Zhang, H. *Small* **2019**, *15*, 1804332.
(31) Wang, L. V.; Hu, S. *Science* **2012**, *335*, 1458–1462.
(32) Ferreira, L. *J. Cell Biochem.* **2009**, *108*, 746–752.
(33) Ricles, L. M.; Nam, S. Y.; Sokolov, K.; Emelianov, S. Y.; Suggs L. J. *Int. J. Nanomedicine* **2011**, *6*, 407–416.
(34) Jokerst, J. V.; Thangaraj, M.; Kempen, P. J.; Sinclair, R.; Gambhir, S. S. *ACS Nano* **2012**, *6*, 5920–5930.
(35) Ricles, L. M.; Nam, S. Y.; Trevi˜no, E. A.; Emelianov, S. Y.; Suggs, L. J. **J. Mater. Chem. B** *2014*, *2*, 8220–8230.
(36) Nam, S. Y.; Ricles, L.; Sokolov, K.; Suggs, L.; Emelianov, S. *Proc. of SPIE* **2011**, 7899.
(37) Qiao, Y.; Gumin, J.; MacLellan, C. J.; Gao, F.; Bouchard, R.; Lang, F. F.; Stafford, R. J.; Melancon, M. P. *Nanotechnol.* **2018**, *29*, 165101.
(38) Kim, T.; Lemaster, J. E.; Chen, F.; Li, J.; Jokerst, J. V. *ACS Nano* **2017**, *11*, 9022–9032.
(39) Yin, C.; Wen, G. H.; Liu, C.; Yang, B. G.; Lin, S. E.; Huang, J. W.; Zhao, P. C.; Hong, S.; Wong, D.; Zhang, K. Y.; Chen, X. Y.; Li, G.; Jiang, X. H.; Huang, J. P.; Pu, K. Y.; Wang, L. D.; Bian, L. M. *ACS Nano* **2018**, *12*, 12201–12211.
(40) Dhada, K. S.; Hernandez, D. S.; Suggs, L. J. *ACS Nano* **2019**, *13*, 7791–7799.

Iron Oxide Nanoparticles

Functional Group	Form	Composition	Particle Size (nm)	Cat. No.
-	nanopowder	-	35 - 45	**746843-5G**
	nanopowder	-	25	**746827-5G**
	nanopowder	-	25	**746835-5G**
	nanopowder	-	60 - 80	**746878-25G**
	nanopowder	-	40 - 60	**746851-25G**
	nanopowder	Fe 55% Ni 45%	<100 (BET)	**677426-5G**
	nanopowder	-	<50 (APS)	**637149-25G** **637149-100G**
	nanopowder spherical	-	50 - 100 (SEM)	**637106-25G** **637106-100G** **637106-250G**
	nanoparticles solution	5 mg/mL in toluene	9 - 11 (TEM; conforms)	**700312-5ML**
	nanoparticles solution	5 mg/mL in toluene	5 ±1 nm (TEM; conforms)	**700320-5ML**
	nanoparticles solution	5 mg/mL in toluene	18 - 22 (TEM)	**700304-5ML**
	dispersion nanoparticles	5 mg/mL in H_2O	4 - 6 (TEM)	**725331-5ML**
	dispersion nanoparticles	5 mg/mL in H_2O	9 - 11 (TEM)	**725358-5ML**
	dispersion nanoparticles	5 mg/mL in H_2O	18 - 22	**725366-5ML**
	nanopowder	-	<50 (BET)	**544884-5G** **544884-25G**
	nanoparticles	15 wt. % in ethanol	≤110	**720712-100G**
	nanoparticles	20 wt. % in H_2O	≤110	**720704-100G**
	dispersion	20 wt. % in water	<5 (DLS)	**796093-100ML**
rhodamine B	dispersion nanoparticles	1 mg/mL in H_2O	10 (TEM)	**900146-2ML**
dextran	dispersion nanoparticles	10 mg/mL in H_2O	5 (TEM)	**900147-2ML**
-	dispersion nanoparticles	5 mg/mL in chloroform	10 (TEM)	**900084-5ML**
PEG	dispersion nanoparticles	1 mg/mL in H_2O	15 (TEM)	**900026-10ML**
amine	dispersion nanoparticles	1 mg/mL in H_2O	25 (TEM)	**900028-10ML**

Functional Group	Form	Composition	Particle Size (nm)	Cat. No.
PEG	dispersion nanoparticles	1 mg/mL in H_2O	25 (TEM)	**900027-10ML**
oleic acid	dispersion nanoparticles	5 mg/mL in toluene	15 (TEM)	**900063-5ML**
-	dispersion nanoparticles	5 mg/mL in H_2O	15 (TEM)	**900043-5ML**
	dispersion nanoparticles	5 mg/mL in H_2O	25 (TEM)	**900042-5ML**
	dispersion nanoparticles	5 mg/mL in H_2O	30 (TEM)	**900062-5ML**
oleic acid	dispersion nanoparticles	5 mg/mL in toluene	25 (TEM)	**900064-5ML**
	dispersion nanoparticles	5 mg/mL in toluene	30 (TEM)	**900081-5ML**
	dispersion nanoparticles	5 mg/mL in chloroform	5 (TEM)	**900082-5ML**
biotin	dispersion nanoparticles	1 mg/mL (in 10 mM PBS buffer)	15 (TMS)	**900037-1ML**
oleic acid	dispersion nanoparticles	5 mg/mL in chloroform	15 (TEM)	**900083-5ML**
	dispersion nanoparticles	5 mg/mL in chloroform	20 (TEM)	**900088-5ML**
	dispersion nanoparticles	5 mg/mL in chloroform	25 (TEM)	**900089-5ML**
	dispersion nanoparticles	5 mg/mL in chloroform	30 (TEM)	**900090-5ML**
streptavidin	dispersion nanoparticles	1 mg/mL in H_2O	10 (TEM)	**900091-1ML**
	dispersion nanoparticles	1 mg/mL in H_2O	15 (TEM)	**900092-1ML**
	dispersion nanoparticles	1 mg/mL in H_2O	20 (TEM)	**900093-1ML**
	dispersion nanoparticles	1 mg/mL in H_2O	25 (TEM)	**900094-1ML**
	dispersion nanoparticles	1 mg/mL in H_2O	30 (TEM)	**900148-1ML**
carboxylic acid	dispersion nanoparticles	5 mg/mL in H_2O	25 (TEM)	**900201-2ML**
amine	dispersion nanoparticles	1 mg/mL in H_2O	15 (TEM)	**900199-10ML**
carboxylic acid	dispersion nanoparticles	5 mg/mL in H_2O	15 (TEM)	**900200-2ML**
NHS ester	nanopowder powder	-	15 (TEM)	**900041-1G**
	nanopowder powder	-	25	**900034-1G**

EDC Conjugation Kits for Iron Oxide Nanoparticles

Functional Group	Form	Composition	Particle Size (nm)	Cat. No.
carboxylic acid	nanoparticles	5 mg/mL	5	**OCNICK05-1KT**
	nanoparticles	5 mg/mL	10	**OCNICK10-1KT**
	nanoparticles	5 mg/mL	15	**OCNICK15-1KT**
	nanoparticles	5 mg/mL	20	**OCNICK20-1KT**
	nanoparticles	5 mg/mL	25	**OCNICK25-1KT**
	nanoparticles	5 mg/mL	30	**OCNICK30-1KT**

SMCC Conjugation Kits for Iron Oxide Nanoparticles

Functional Group	Form	Composition	Particle Size (nm)	Cat. No.
amine	nanoparticles	5 mg/mL	5	**OCNIAK05-1KT**
	nanoparticles	5 mg/mL	10	**OCNIAK10-1KT**
	nanoparticles	5 mg/mL	15	**OCNIAK15-1KT**
	nanoparticles	5 mg/mL	20	**OCNIAK20-1KT**
	nanoparticles	5 mg/mL	25	**OCNIAK25-1KT**
	nanoparticles	5 mg/mL	30	**OCNIAK30-1KT**

Iron Oxide Incorporated Conjugated Polymer Nanoparticles

Fluorescence Emission (nm)	Concentration	Cat. No.
λ_{em} = 475	100 µg/mL in H_2O	**905054-250UL**
λ_{em} = 510	100 µg/mL in H_2O	**905038-250UL**
λ_{em} = 680	100 µg/mL in H_2O	**904996-250UL**
λ_{em} = 550	100 µg/mL in H_2O	**905046-250UL**

MilliporeSigma
400 Summit Drive
Burlington, MA 01803

MATERIALS RESEARCH SOCIETY MID-CAREER RESEARCHER AWARD

The Mid-Career Researcher Award recognizes exceptional achievements in materials research made by mid-career professionals. It is not limited to the method of characterization or the class of materials observed.

Zhenan Bao

baogroup.
stanford.edu

Zhenan Bao

Affiliation: Stanford University

For pioneering contributions and conceptual developments to organic electronics and skin-inspired electronics

Zhenan Bao is Department Chair and K.K. Lee Professor of Chemical Engineering, and by courtesy, Professor of Chemistry and Professor of Material Science and Engineering at Stanford University. Bao founded the Stanford Wearable Electronics Initiate (eWEAR) in 2016 and serves as the faculty director. Prior to joining Stanford in 2004, she was a Distinguished Member of Technical Staff in Bell Labs, Lucent Technologies from 1995-2004. Bao received her Ph.D in Chemistry from the University of Chicago in 1995.

She has over 550 peer-reviewed publications and over 65 US patents with a Google Scholar H-Indes of >170. Bao is a member of the National Academy of Engineering and the National Academy of Inventors.

In 2015, Bao was selected by Nature's "10 people who mattered" as a "Master of Materials" for her work on artificial electronic skin. She was awarded the inaugural ACS Central Science Disruptor and Innovator Prize in 2020 and the Gibbs Medal by the Chicago session of ACS both in 2020.

Over the past decade, Bao's group has developed material design concepts that add skin-like functions to organic electronic materials without compromising their electronic properties. These new materials and devices hold great promise for a range of innovative applications in medical devices, robotics and wearable electronics.

MRS acknowledges the generosity of MilliporeSigma in endowing this award.